

Convolutional Neural Networks and Volcano Plots: Screening and Prediction of Two-Dimensional Single-Atom Catalysts for CO₂ Reduction Reactions

Haoyu Yang¹, Juanli Zhao², Qiankun Wang³, Bin Liu², Wei Luo⁴,
Ziqi Sun^{1,*}, and Ting Liao^{5,*}

¹*School of Chemistry and Physics, Queensland University of
Technology, George Street, Brisbane, QLD 4000, Australia*

²*School of Materials Science and Engineering, Shanghai University,
Shanghai, China*

³*School of Computer Science and Engineering, Southeast
University, Nanjing, China*

⁴*College of Materials Science and Engineering, Institute of
Functional Materials, Donghua University, Shanghai, China*

⁵*School of Mechanical Medical and Process Engineering,
Queensland University of Technology, George Street, Brisbane,
QLD 4000, Australia*

*Corresponding author: ziqi.sun@qut.edu.au

*Corresponding author: t3.liao@qut.edu.au

Abstract

Single-atom catalysts (SACs) have emerged as pivotal frontiers for catalyzing a myriad of chemical reactions, yet the diverse combinations of active elements and support materials, the nature of coordination environments, elude traditional methodologies in searching optimal SAC systems with superior catalytic performance. Herein, by integrating multi-branch Convolutional Neural Network (CNN) analysis models to hybrid descriptor based activity volcano plot, two-dimensional (2D) SAC system composed of diverse metallic single atoms anchored on six type of 2D supports, including graphitic carbon nitride ($\text{g-C}_3\text{N}_4$), nitrogen-doped graphene, graphene with dual-vacancy, black phosphorous, boron nitride (BN), and C_2N , are screened for efficient CO_2RR . Starting from establishing a correlation map between the adsorption energies of intermediates and diverse electronic and elementary descriptors, sole singular descriptor lost magic to predict catalytic activity, including d-band center. Deep learning method utilizing multi-branch CNN model therefore was employed, using 2D electronic density of states (eDOS) as input to predict adsorption energies. Hybrid-descriptor enveloping both C- and O-types of CO_2RR intermediates was introduced to construct volcano plots and limiting potential periodic table, aiming for intuitive screening of catalyst candidates for efficient CO_2 reduction to CH_4 . The eDOS occlusion experiments were performed to unravel individual orbital contribution to adsorption energy. To explore the electronic scale principle governing practical engineering catalytic CO_2RR activity, orbitalwise eDOS shifting experiments based on CNN model were employed. The study involves examining the adsorption energy and, consequently, catalytic activities while varying supported single atoms. This work offers a tangible framework to guide both theoretical screening and experimental synthesis, thereby paving the way for systematically designing efficient SACs.

1 Introduction

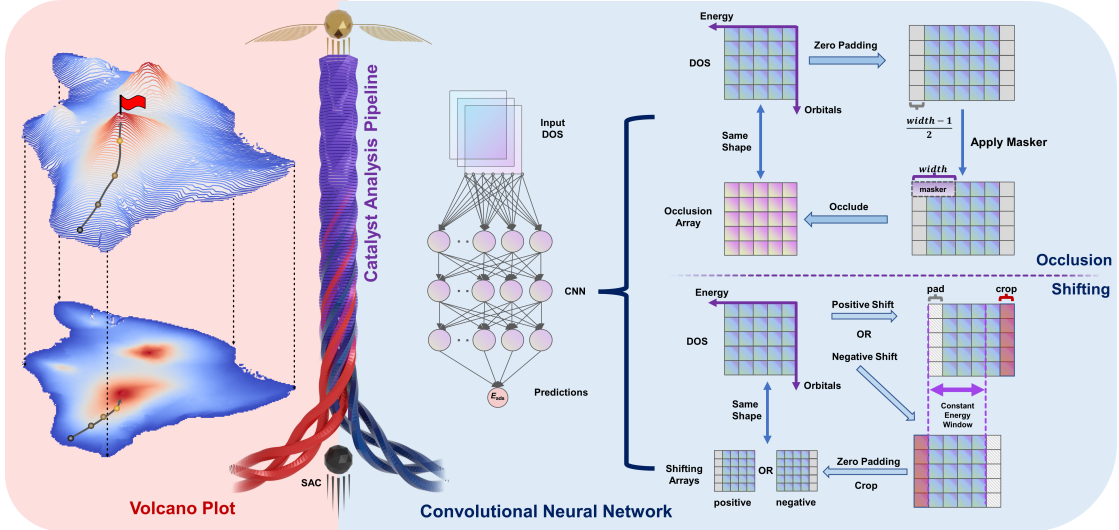


Figure 1: Catalyst performance analysis pipeline integrating volcano plots and CNN. The figure demonstrates the integrated usage of volcano plots for predictive assessment of existing catalysts, and the utility of CNNs to predict and modulate adsorption energies E_{ads} using eDOS as input. eDOS occlusion and shifting experiments are conducted to extract chemical information from CNN model.

Electrochemical CO₂RR stands as a promising avenue for long-term seasonal energy storage [14] and mitigating excess CO₂ in the atmosphere.

Despite decades of research, metallic copper remains a leading CO₂RR electrocatalyst for hydrocarbon production [51], albeit burdened by substantial overpotential and low faradic efficiency and poor operational stability [9, 42]. In this regard, supported SACs have displayed remarkable activity and selectivity across various catalytic reactions [63, 69], leveraging their unique electronic properties and coordination environment. To date, experimental studies have primarily focused on two-electron reduction products due to the facile release of gaseous CO [6, 28, 55]. Consequently, there is a pressing need to modulate the electronic structure of single-atom sites to enable hydrocarbon production at reduced overpotential.

The challenge towards effective catalysts design lies in understanding the reaction mechanisms. Experimental determination of these mechanisms remains challenging due to the complexity of in situ spectroscopic detection of reaction intermediates [74]. Computational modeling, particularly methods based on quantum mechanics (QM) such as density functional theory (DFT), allows for the profiling

the energetics of intermediates and unveils structure-activity relationships for identified active sites [17, 7], contributing to understanding of reaction mechanisms. However, the high computational cost of QM methods restricts the accessible catalyst space [27, 10, 20].

In this context, researchers have explored descriptor-based methods to circumvent QM calculations and establish direct correlations between target properties and electronic factors, commonly referred to as descriptors or features. Traditional methods of crafting descriptors, as seen in the d-band model of Hammer and Nørskov [22], necessitate meticulous selection of chemical properties based on chemical knowledge and are inherently case-dependent [29]. Particularly in the case of SACs, the relationship is intricate, rendering manual crafting inadequate [24, 61]. To streamline this featurization process, we employed CNNs, which autonomously derive a hierarchical representation directly from the eDOS [62, 58, 38]. This approach accurately maps to the activity space, negating the need for manual crafting of descriptors and providing a more efficient method to understand and establish the structure-mechanism-activity relationship for electrochemical reactions.

In this study, we introduced a catalyst performance analysis pipeline (Figure 1) integrating a customized CNN model and volcano plots. Our CNN model accurately estimated the adsorption energies, the activity descriptor, from the eDOS of 2D materials supported single metal catalysts. Evaluations on the adsorption energies of nine intermediates along CO₂RR and competing hydrogen evolution reaction (HER) as well yielded prediction mean absolute errors (MAEs) at the level of 0.1 eV, which is well aligned with the precision of conventional DFT calculations [32, 40, 67]. This result validated the capability of current CNN model to accurately capture intricate spatial information from eDOS. Building on this, we introduced an orbitalwise eDOS occlusion experiment was adopted afterwards inspired from the occlusion technique widely used in computer vision and pattern recognition applications. Systematic eDOS experiment was performed to elucidate orbitalwise contributions to the adsorption energies at different energy levels, which produced consistent outcome from Crystal Orbital Hamilton Population (COHP) analysis and real-space wavefunction visualization. All these results justified the proficiency of CNN model on identifying the dominant orbitals for adsorbate-substrate interactions. Furthermore, orbital-wise eDOS shifting experiment, exploring the impact of orbital-wise eDOS shifting on the adsorption behavior of studied catalysts were performed.

Simultaneously, we incorporated the volcano plots into the catalysis performance analysis pipeline. Besides offering intuitive analysis of catalyst activities (represented by the elevation of volcanoes), volcano plots points to the directions on how effort can be exerted to identify promising catalyst candidates. Built upon

scaling relations [54], we introduced a hybrid-descriptor scheme incorporating both C- and O-centered species. The scaling coefficient of determination (R^2) was increased by 0.1387 using hybrid descriptor, which demonstrate an improved prediction accuracy compared to the well documented single descriptor based method.

In summary, we introduced a catalyst performance analysis pipeline by integrating CNN and volcano plot analysis, using CO₂RR as an example proof of concept. The CNN, which correlates eDOS with activity descriptors, establishes a robust electronic structure-activity relationship. Notably, it is capable to predict the influence of eDOS disturbances, caused by either alloying, strain, or defects [48, 4, 39], to modulate the catalytic activity of materials, which will offer insights into the intrinsic mechanism for rationalized catalyst optimization strategies. Advancing the current volcano plot method, the involvement of CNN models in catalyst performance analysis pipeline holds enormous promise for advanced exploration of catalysts with superior performance.

2 Results

2.1 Adsorption energy prediction from electronic density of states with convolutional neural network

Originating from the pioneering work of Hammer and Nørskov [23], the d-band center model has emerged as a successful paradigm for employing descriptor to understand and predict the adsorption behavior on transition metal surfaces. To investigate alternative electronic and elementary descriptors that may serve as more suitable substitutes for the d-band center model in the context of SACs, we performed Kendall rank correlation analysis to account for both linearity and non-linearity [30]. The correlation coefficient map, as presented in Figure 2a, highlighted the d-band center as the most informative descriptor with a Kendall's τ coefficient of -0.33, and followed by the vacuum level and electronegativity. However, d-band center alone does not suffice for accurate predictions of intermediate adsorption energy as illustrated in the scatter plot Supplementary Figure 23, and therefore, refinements are imperative. Unlike bulk transition metal surfaces, where the variations in the d-band centre account for the majority of the adsorption energy variations [48, 60], the unique structure of SACs introduces more variables rather than d-band center that are intrinsically correlated with the variations of adsorption energy. This finding also interpreted that in some reported prior studies, indicating that depending solely on the d-band center may be insufficient for accurate adsorption energy predictions in the context of SACs [59, 19, 13, 70, 25]. As a result, the development of a method tailored specifically for catalysts like SACs becomes essential.

In our study, we employ CNN, a renowned deep learning method proficient in capturing spatial hierarchy from matrix-like data, such as the eDOS. Notably, CNN's autonomy from prior knowledge and human intervention during feature extraction renders it more efficient than traditional machine-learning methods. Our approach harnesses the entire 2D eDOS with a multi-branch CNN model. Figure 2b and Figure 2c delineate the model and its branches. The workflow involves processing the entire 2D eDOS as input, segregating orbitals into branches, and directing the concatenated outputs through another convolutional block, which generates the adsorption energy prediction. Sharing learnable parameters across branches optimizes computational efficiency. By leveraging the CNN model, we predicted adsorption energies from the eDOS of supported single atoms, and validated through parity plots (Figure 2d-m). The model predicts adsorption energies across nine species within the CO₂RR process and competing HER side reaction, attaining an averaged MAE of 0.06 eV. This MAE aligns with the established precision of DFT methods, which typically range between 0.1-0.2 eV concerning experimental measurement [67, 32, 40]. The full list of prediction errors is available

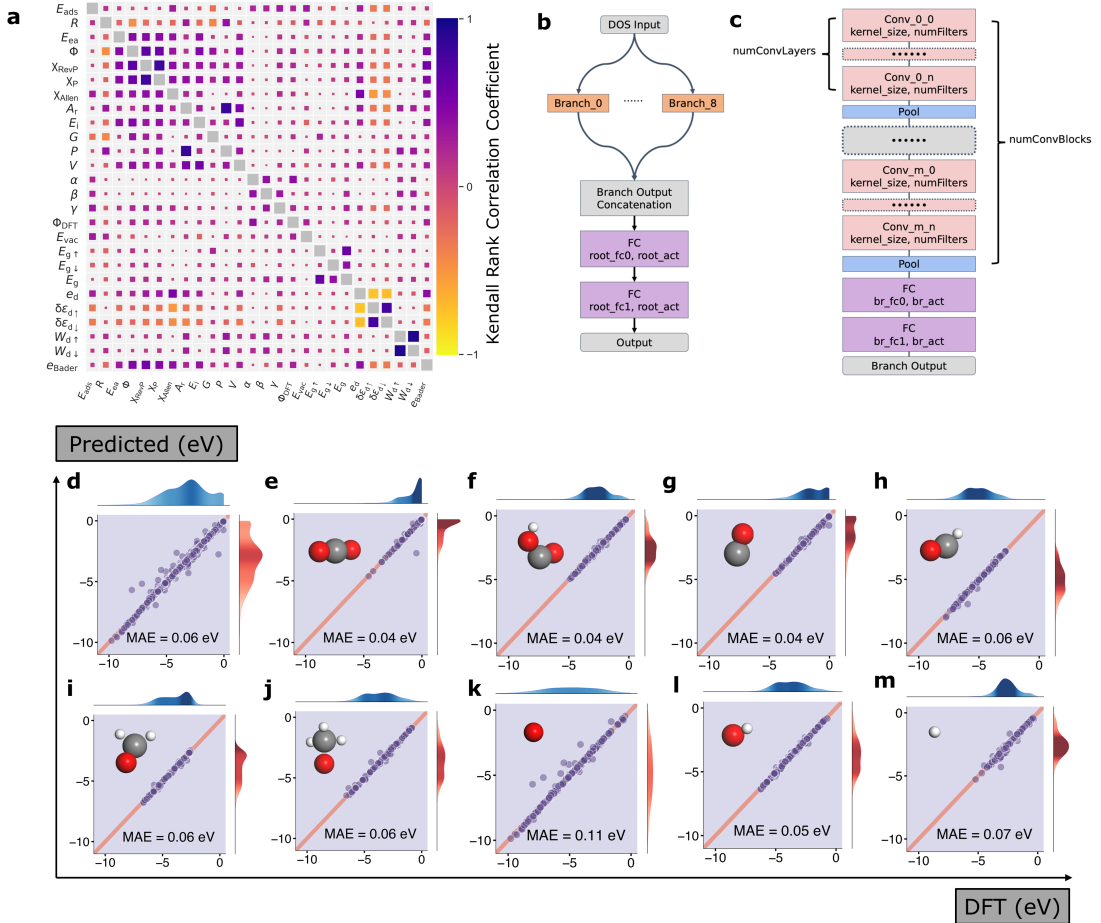


Figure 2: CNN for electronic density of states. **a.** Kendall rank correlation coefficient map illustrating the correlation between adsorption energy and other electronic and elementary descriptors. Definitions of the notations are provided in Supplementary section II.2. **b-c.** Architectural of (b) the root and (c) each branch of the CNN model. The architecture stays consistent across individual branches. **d-m.** Parity plots demonstrating the performance of the CNN model across nine adsorbates: (d) all adsorbates, (e) CO₂, (f) COOH, (g) CO, (h) CHO, (i) CH₂O, (j) OCH₃, (k) O, (l) OH, and (m) H. The augmentation data are not displayed in these plots, nor included in MAE evaluations. Kernel density estimate results are shown along the top and right sides of the main plot, representing DFT calculations and CNN model prediction distributions, respectively.

in Supplementary section II.4. These results confirm the CNN model’s ability to predict adsorption energies from eDOS input. Moreover, they suggest the potential for predicting adsorption energies for SACs using eDOS, although this would demand more sophisticated feature engineering techniques.

In terms of adsorption energy prediction, the CNN model maintained consistency across diverse elemental compositions and varied adsorption strengths. It handled species containing oxygen, hydrogen, and carbon atoms equally well, spanning an adsorption energy range from 0 to 10 eV. Significantly, after training the CNN model, making predictions (inferences) scales only linearly with system size and demands considerably less computational resources compared to DFT calculations [8]. Conversely, unlike QM based methods, which could generate reasonably precise energy estimation for individual candidates, CNN relies on extensive datasets to ensure reliable predictions. In our case, the original dataset comprised 2052 samples, leading to a CNN model with a validation MAE of 0.3725 eV. In pursuit of enhanced prediction accuracy, we proposed a data augmentation method detailed in the Methods section. This augmentation resulted in an expanded dataset of 12312 samples, enhancing prediction performance with a reduced validation MAE of 0.1736 eV. Comparatively, our CNN model diverges from prior attempts, notably Fung’s pioneer work [18], by requiring only the eDOS of supported single metal atom alone and adsorbate. This revision eliminated the necessity for a complete set of substrate and adsorbate eDOS and significantly reduced computational cost. We foresee the potential in the applicability of our method to diverse species and electrocatalytic reactions, given the availability of comprehensive datasets. The strength of our CNN model lies in its freedom from element- or adsorbate-specific parameters, relying solely on eDOS as input. This adaptability opens up the possibility for its utilization in a wide array of electrocatalytic studies.

2.2 Hybrid descriptors enabled volcano plot for catalyst analysis

Catalyst activity volcano plots, built upon the scaling relations proposed by Peterson and Nørskov’s [54], goes beyond assessment of candidatures’ energetics only but to provide informative guidance on discovering catalysts candidates with superior performance [3, 12]. Our endeavor to improve the accuracy of volcano plots leads to the development of the hybrid-descriptor, which encompasses both C- and O- bonding types of CO₂RR intermediates within the scaling relations. This adaptation arose from the intuition that most CO₂RR intermediates are featured with both bonding types rather than any single one in dominance. By integrating both bonding featured descriptors into the hybrid approach, we found the R^2

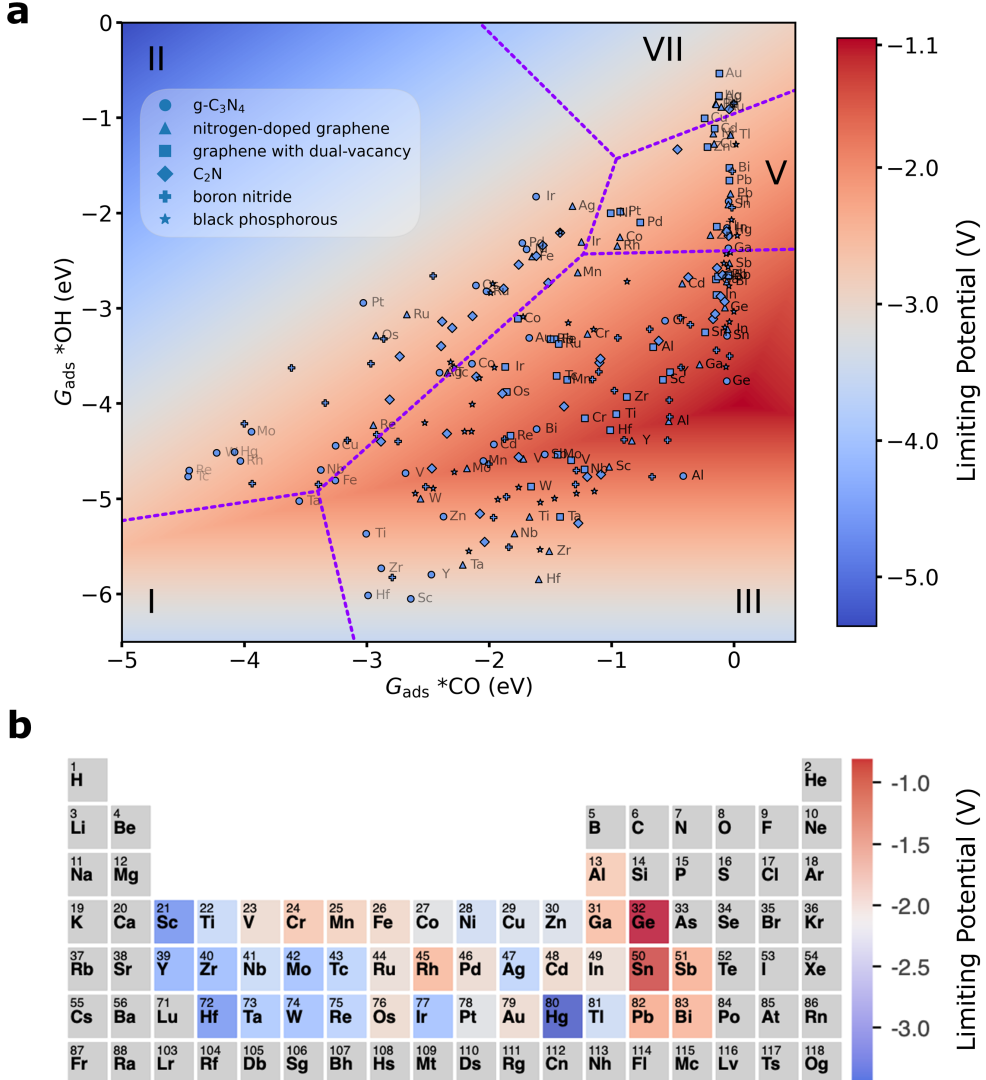


Figure 3: Limiting potential volcano plot and periodic table. **a.** Limiting potential volcano plot computed from hybrid-descriptor-based linear scaling relations at potential of -0.17 V vs SHE. In the plot, the circle, triangle, square, diamond, plus, and star symbols represent metals supported on $\text{g-C}_3\text{N}_4$, nitrogen-doped graphene, graphene with dual-vacancy, black phosphorous, BN, and C_2N , respectively. Dotted purple lines delineate regions representing rate-determining steps, with roman numerals denoting the respective RDS for each region. The reaction steps are defined in Equation (1) to Equation (8). **b.** Limiting potential periodic table illustrating the theoretical activity of single metal atom catalysts supported on $\text{g-C}_3\text{N}_4$.

was increased by 0.1387. Detailed information about the scaling parameters and performance enhancements are provided in Supplementary section I.5 and Supplementary Figure 15. This improvement to some extent underscored our premise that CO₂RR intermediates typically exhibit chemical similarities encompassing both O- and C-type descriptors. After taking this dual nature into consideration, our hybrid-descriptor method can evaluate the intermediates adsorption energies more accurately. Importantly, the introduction of hybrid descriptors is computationally affordable compared to DFT methods, as it involves only a set of linear regressions to identify the optimal mixing ratio, as elaborated in the Methods section.

Expanding upon the revised scaling relations, we introduce an activity volcano plot and a rate-determining step (RDS) volcano plot for the CO₂RR process, shown in Figure 3a and Supplementary Figure 16. Given that HER is a key competing reaction with CO₂RR [21], we also incorporated a selectivity volcano plot, presented in Supplementary Figure 17, to offer a comprehensive analysis of catalyst candidates. In adherence to Peterson and Nørskov's original framework [54], our choice of x and y axes descriptors aligned with $G_{\text{ads}*\text{CO}}$ and $G_{\text{ads}*\text{OH}}$. Further elaboration on how the limiting potentials were evaluated across the volcano plot can be found in the Methods section. Among the candidatures explored, Ge@g-C₃N₄ emerged as the most promising catalyst, demonstrating theoretical activity at a limiting potential of -1.2126 eV. Notably, the observed selectivity trend paralleled the activity trend, suggesting that catalysts exhibiting high theoretical activity are also resistant to HER side reactions. The RDS volcano plot (Supplementary Figure 16) indicated protonation of *CO as the rate-determining step for nearly optimal candidates. Moreover, the activity volcano plot predicted an optimal catalyst featuring a theoretical limiting potential of -1.0516 V, at $G_{\text{ads}*\text{CO}}$ of 0.0589 eV and $G_{\text{ads}*\text{OH}}$ of -4.0075 eV, positioned at the right-center of the volcano plot. Results from RDS volcano plot indicate that protonation of *CO likely serves as the RDS for CO₂RR. Consequently, it should be the focal point for future catalyst designs. The activity and selectivity volcano plots imply that enhancing theoretical activity could be achieved by decreasing CO affinity while increasing OH affinity with the catalysts. This result suggests a perspective: weak binding of CO to the catalyst surface might facilitate the rotation of C-O backbone from the “upright” configuration in *CO to the “horizontal” orientation in *CHO [53], and therefore facilitating dynamics and protonation of the *CO species.

The volcano plot offers an intuitive analysis of the reaction energetics and provides insights into the mechanisms of the reaction. While the volcano plot provides a broad overview, it lacks the ability to delve into lower-level explanations rooted in electronic structures, where detailed electronic interactions and specific bonding mechanisms remain beyond its scope. Despite its limitations, the volcano

plot serves as a useful tool for identifying focal elementary steps in the reaction pathway that demand closer attention during catalyst design. It also highlights directions for further catalyst refinement, and can also be integrated with the shifting experiment discussed later to optimize existing catalysts.

Additionally, we mapped the theoretical limiting potentials of the analyzed catalyst candidates onto periodic tables, shown in Figure 3b and Supplementary Figure 18 to Supplementary Figure 22. Our analyses do not reveal consistent trends within groups or periods, nor did they exhibit evident patterns across substrates. These observations suggest intricate interactions between supported metal atoms and substrates. The absence of straightforward trends underscores the need for nuanced explorations in understanding these interactions like the CNN model.

2.3 Validation of CNN predictions

Historically, interpretability has posed challenges for deep learning methods, often rendering their inner workings akin to black boxes [73, 72, 57]. The occlusion technique, widely utilized in Computer Vision [71, 34, 64], involves systematically masking sections of the input matrix to assess their impact on the final prediction score. In our work, we introduce an orbitalwise occlusion method to discern individual orbital contribution to adsorption energy within the CNN model, drawing inspiration from Fung’s pioneer integration of this technique into eDOS analysis [18]. In this work, occlusion experiments involve orbitalwise masking specific eDOS, which are then fed into the CNN model to observe resulting disturbance in adsorption energy. A visual representation of this process can be found in Supplementary Figure 26. Conceptually, this experiment simulates the effect of shielding electronic states, allowing investigation of the potential contribution to adsorption energy from these states. Additionally, we attempted to extract the planewave coefficients of Kohn-Sham orbital for wavefunction visualization. This validation step was undertaken to confirm the spatial distribution of the orbitals pinpointed by the occlusion experiments.

To validate our method, we conducted occlusion experiments on Cr@g-C₃N₄, Co@g-C₃N₄ and Cu@g-C₃N₄. Each of these supported metals possesses 3d subshells with different electronic configurations: half-filled, partially filled and fully filled, allowing us to test the universality of our approach. The results of the occlusion experiment on the supported Cr single atom in Cr@g-C₃N₄ are given in Figure 4a. The $d_{x^2-y^2}$ orbital emerges as dominant in CO interaction. Shielding electrons centered around -2 eV significantly alter the adsorption energy, indicating the potency of this orbital. The real-space wavefunction visualization in Figure 4d corroborates these findings, highlighting the interaction between the $d_{x^2-y^2}$ orbital of single metal atom and the adsorbate. This suggests the $d_{x^2-y^2}$ orbital of supported Co predominantly influence the interaction with CO, and thus shielding

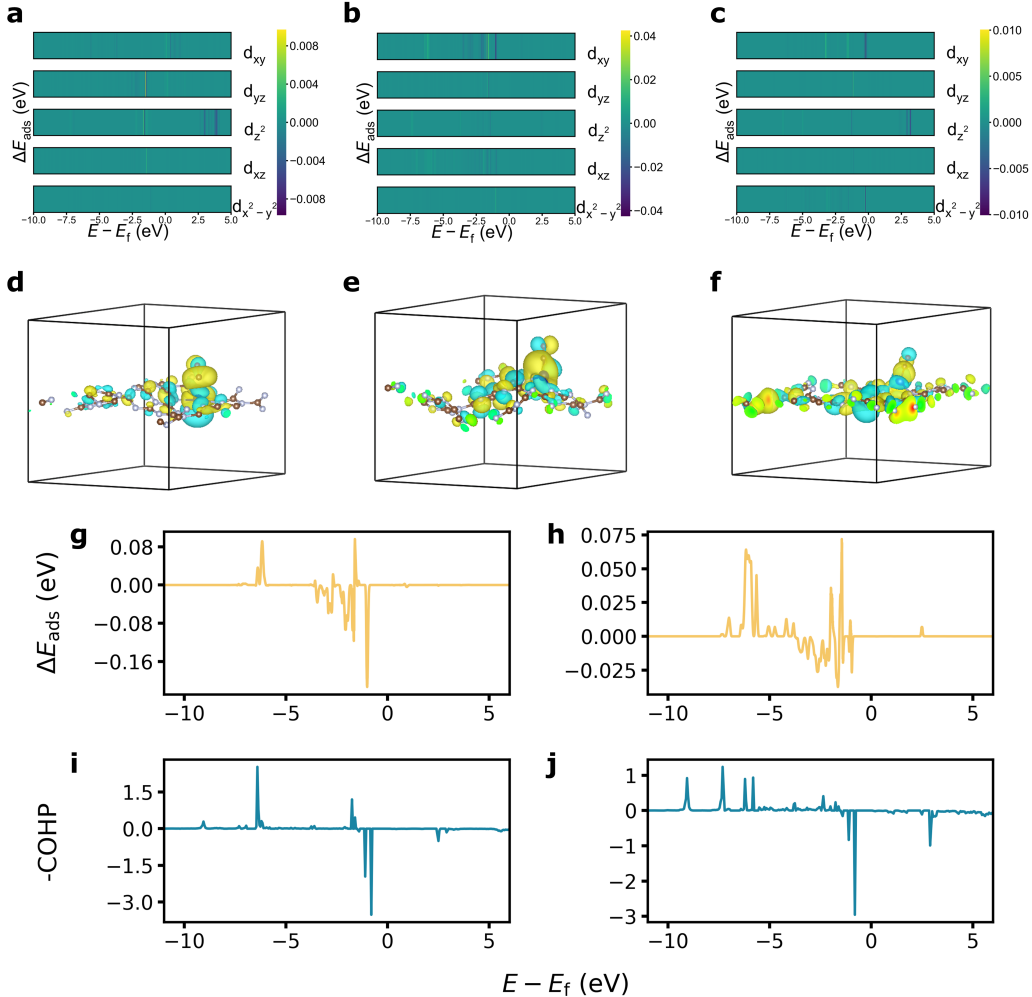


Figure 4: Validation of CNN predictions. **a-c,** The eDOS occlusion experiment results for (a) Cr of Cr@g-C₃N₄, (b) Co of Co@g-C₃N₄ and (c) Cu of Cu@g-C₃N₄. eDOS occlusion experiments were conducted on the initial states of CO adsorption process. **d-f,** Real-space wavefunction visualization for (d) Cr $d_{x^2-y^2}$ orbital of Cr@g-C₃N₄, (e) Co d_{xy} orbital of Co@g-C₃N₄ and (f) Cu d_{xy} orbital of Cu@g-C₃N₄. Wavefunction visualizations were performed on the final states of CO adsorption process. The yellow and aqua colors represent areas of positive and negative Kohn-Sham orbital coefficients, respectively. **g-j,** Occlusion experiment results for (g) d_{xy} orbital and (h) d_{xz} orbital for Co of Co@g-C₃N₄. COHP analysis for (i) d_{xy} orbital and (j) d_{xz} orbital for Co of Co@g-C₃N₄, performed between Co and all adsorbate atoms in the final states of CO adsorption process.

electrons from this orbital markedly disturb the adsorption energy. Additionally, occlusion experiments were performed on the Co d_{xy} orbital of Co@g-C₃N₄ (Figure 4b) and the Cu d_{xy} orbital of Cu@g-C₃N₄ (Figure 4c). In both cases, the d_{xy} orbital was identified as the dominant contributor. While identifying the dominant orbital is crucial, these findings also suggest that interactions with adsorbates occurring out-of-plane are influenced by in-plane orbitals as well. Importantly, it becomes evident that d orbitals do not universally impact interactions with adsorbates, emphasizing the need for case-specific discussions.

To validate the chemical relevance of predictions made by CNN model, we conducted COHP analysis, a theoretical bond-detecting tool used to identify bonding and anti-bonding contributions to band-structure energy [11]. In this research, interactions between the supported metal atom and atoms within a 5 Å radius were calculated to understand its bonding environment, as detailed in the Methods section. The results of the occlusion experiment on the Co d_{xy} orbital of Co@g-C₃N₄, identified as the dominant orbital via occlusion experiments, were compared with the COHP analysis, as shown in Figure 4g and Figure 4i. The occlusion experiment pinpointed strong metal-adsorbate interactions at energy levels of -1 eV and -6.3 eV, which were confirmed by the COHP analysis. We then investigated the non-dominant Co d_{xz} orbital, and the COHP analysis highlighted interactions at -1 eV and -6.5 eV, aligning with the findings from the occlusion experiments.

In summary, orbitalwise occlusion experiments provide chemical interpretations into deep learning models, enhancing their interpretability. Furthermore, these occlusion results are readily understandable to chemists, enabling the identification of orbitalwise contributions to the adsorption process.

2.4 eDOS shifting experiments for prediction of better catalysts

While CNN models excel in prediction of the activity of catalyst candidates directly from eDOS, volcano plots point out directions leading to better catalysts. Exploring potential disturbances to adsorption energies and aiming to shift existing catalyst candidates closer to the peak of the activity volcano plot presents an intriguing avenue of investigation. In this work, we introduce an orbitalwise shifting experiment to explore the impact of orbitalwise eDOS shifting on adsorption behavior. The experiment involved shifting eDOS along the energy axis, and the CNN model was deployed to predict the resultant disturbance in adsorption energy for each shifting operation. Focusing on all Period 4 metal elements examined in this study, we analyzed the effects of eDOS shifting. To induce a moderate disturbance, we selected the energy range of -1 to 1 eV, and a shifting resolution of 0.005 eV/step was chosen to align with the eDOS calculation resolution.

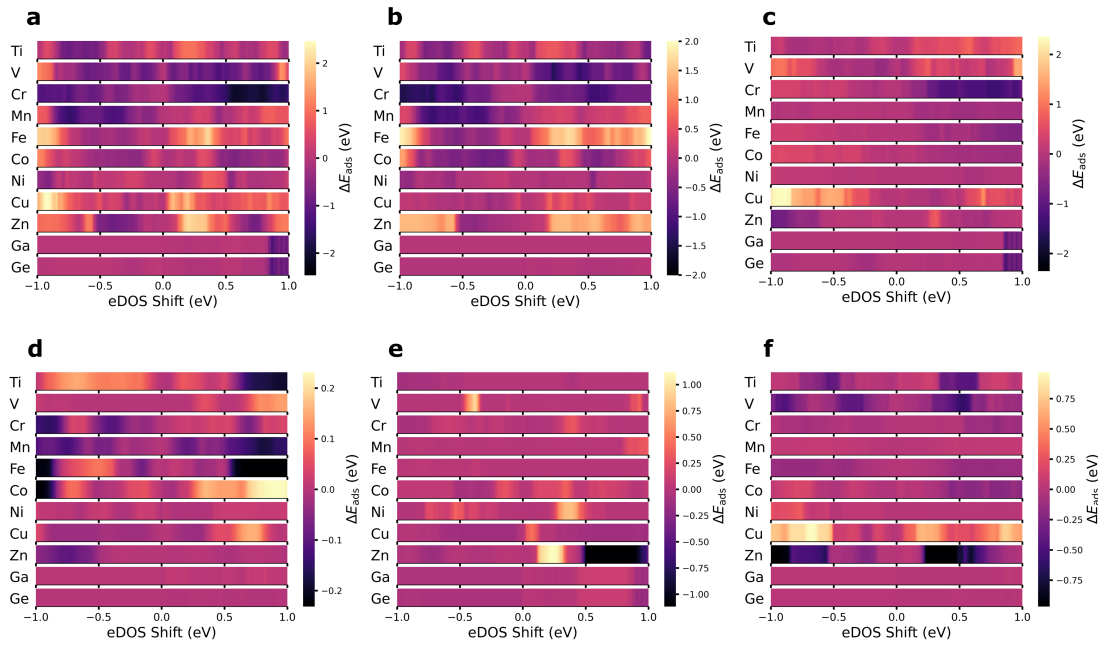


Figure 5: eDOS shifting experiments. Impact of orbitalwise eDOS shifting on CO adsorption energy, as predicted by the CNN model, for single metal atom catalysts supported on g-C₃N₄. The disturbances caused by shifting of (a) entire d , (b) d_{xy} , (c) d_{yz} , (d) d_{z^2} , (e) d_{xz} and (f) $d_{x^2-y^2}$ orbitals are illustrated. The shifting step size corresponds to the energy resolution of the eDOS, and is 0.005 eV in this study. A positive eDOS shift indicates a shift towards higher energy levels, and vice versa.

Figure 5 illustrates that supported Ga and Ge, the sole p-block metals in our study, exhibited no response to d orbital shifting. This observation is consistent with their lack of d-electrons in their valence shells, reinforcing the reliability of our shifting experiments. We also investigated potential disturbance from p orbital shifting, as shown in Supplementary Figure 36 and found no significant response. This implies that Ge@g-C₃N₄ holds promise as a CO₂RR electrocatalyst, given its high activity and resilience to electronic structure disturbances. Nevertheless, fine-tuning its performance through eDOS modulation might pose a challenge. In contrast, supported Fe, Cu and Zn display strong sensitivity to eDOS shifting. Interestingly, the adsorption energy consistently shifted towards more positive values, indicating a weakening of the catalyst-adsorbate interaction, regardless of the shifting direction within the investigated energy range. This underscores the intricate interplay between the supported metal atom and the substrate, emphasizing the necessity of a tool like the CNN model to predict such disturbances. Supported Cr exhibited a contrary response to eDOS shifting, strengthening the interaction with the CO adsorbate regardless of the shifting direction. Supported Ti, V, Co and Ni showed weak response to eDOS shifting, suggesting the need for alternative methods beyond manipulating their eDOS to regulate their interactions with CO adsorbate.

In summary, shifting experiments offer a valuable means to predict the potential disturbances in adsorption behavior resulting from eDOS shifting, a task that is challenging to accomplish directly within the DFT framework. However, it's important to note that achieving the predicted shifting in actual theoretical or experimental scenarios may not be easily accessible. Skillful manipulation of the electronic structure of catalyst candidates would be required, presenting a practical challenge. In contrast to prior studies on bulk metals [18], wherein the adsorption energy exhibits a continuous shift with eDOS variations, the response of SACs is notably discrete. These responses manifest as isolated peaks throughout the shifting range, attributed to the distinctive structure of SACs. Despite this challenge, having a tool that can predict the potential impact of eDOS shifting is advantageous for the theoretical design of SACs.

3 Methods

3.1 DFT calculations

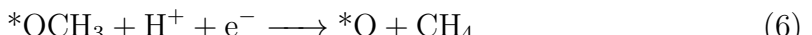
Spin-polarized density functional theory calculations were performed using the Vienna Ab initio Simulation Package (VASP) version 5.4.4 [36, 35, 37] to optimize geometries and determine the electronic structure. The Perdew-Burke-Ernzerhof (PBE) functional [36] within the generalized gradient approximation (GGA) [52] was utilized to describe the electron-ion interactions and electronic exchange correlations. Kohn-Shan equations were approached employing a plane-wave basis set with a cut-off energy of 440 eV. Geometry optimizations were performed using Γ -Centered K-point meshes of $(2 \times 2 \times 1)$ until the force on each atom fell below 0.02 eV \AA^{-1} . Electronic structure calculations utilized denser K-point meshes of $(3 \times 3 \times 1)$ and employed self-consistent field (SCF) methods.

3.2 Catalyst models

Supported SACs were modelled by anchoring individual metal atoms onto various 2D substrates, including g-C₃N₄, nitrogen-doped graphene, graphene with dual-vacancy, black phosphorous, boron nitride, and monolayer C₂N. The specific single metal atoms studied are outlined in Supplementary Figure 6. To prevent interactions between adjacent images along the z-axis, vacuum layers of 15 Å were introduced.

3.3 CO₂RR pathway

The C1 production CO₂RR pathway, as initially described by Peterson et al. [53] and later confirmed by Jiao et al. [26] for g-C₃N₄ based SACs, involves the following elementary steps. Asterisks (*) indicate species adsorbed on the SAC surfaces:



3.4 Free energy calculations

Free energies were computed from electronic energies by considering thermal corrections, incorporating normal mode analysis of all degrees of freedom of adsorbates. The free energy G was calculated using the formula:

$$G = E + E_{\text{ZPE}} - TS \quad (9)$$

where G represents the free energy, E denotes electronic energy, E_{ZPE} is the zero-point energy, T represents temperature in Kevin, and S stands for entropy. Detailed information regarding these corrections can be found in Supplementary section I.3.

The computational hydrogen electrode (CHE) model [53, 49] was employed to introduce potential dependence. At the reference electrode surface, the reaction



is in equilibrium, allowing the calculation of the chemical potential of the electron-proton pair as:

$$\mu(\text{H}^+) + \mu(\text{e}^-) = \frac{1}{2}\mu(\text{H}_{2(\text{g})}) - eU \quad (11)$$

For the external potential U applied, the change in free energy (ΔG) was determined using the equation:

$$\Delta G_n(U) = \Delta G_n(U = 0) + neU \quad (12)$$

Here, μ represents chemical potential, U signifies the external potential applied, n represents the number of proton-electron pairs transferred, and e denotes the elementary charge.

3.5 Hybrid descriptor for volcano plots

Hybrid descriptors incorporate both descriptors within a single equation, enhancing the accuracy of scaling relationship with minimal computational overhead, as demonstrated in Supplementary Figure 15 and Supplementary section I.5. Comprehensive analyses are presented Supplementary section I.5. This leads to the formulation of the scaling relation:

$$G_{\text{ads}}Z = k[\theta^*G_{\text{ads}}\text{CO} + (1 - \theta^*)G_{\text{ads}}\text{OH}] + c_Z \quad (13)$$

Here, θ represents the mixing ratio of the CO descriptor, Z denotes any adsorbate, and k and c_Z are adsorbate-specific scaling parameters. The optimal mixing ratio

θ is determined through iterative exploration across the range, utilizing a step length of 0.01.

13 could be simplified to a more general form:

$$G_{\text{ads}}Z = a_Z G_{\text{ads}}\text{CO} + b_Z G_{\text{ads}}\text{OH} + c_Z \quad (14)$$

Here, a_Z , b_Z , c_Z are adsorbate-specific parameters.

Consequently, the limiting potential U_L is entirely determined by two descriptors through the following equation:

$$U_L = -\frac{\max\{\Delta G_i\}}{e} \quad (15)$$

Where ΔG_i represents the free energy change of reaction step i.

This approach simplifies the theoretical performance assessment of any catalyst within the scope of our research to only two descriptors: $G_{\text{ads CO}}$ and $G_{\text{ads OH}}$. This method offers a visual representation of the high-dimensional optimization challenge. To aid visualization, a 2D mesh grid is established, enabling vectorized assessments of limiting potentials across the descriptor value ranges. At each grid point, the limiting potential is computed using Equation (15).

3.6 CNN architecture and hyperparameter tuning

We designed our CNN architecture drawing inspiration from its successful implementation in tasks involving electrocardiogram signal classification [66], as illustrated in Figure 2b and Figure 2c. This multi-branched CNN comprises nine branches tailored to handle eDOS orbitals while ensuring a reduced memory footprint.

The effectiveness of neural network models is intricately tied to the choice of hyperparameters. To identify the optimal set of hyperparameters, we employed Hyperband [41], a modern and parallelizable bandit-based optimization algorithm. The search space for hyperparameters is detailed in Supplementary section II.4, and the resulting optimal hyperparameters are presented in Supplementary section II.4.

3.7 Data augmentation and CNN model training

To enhance the generalizability and robustness of the our CNN model, and achieve comprehensive coverage of the chemical space [68], we applied data augmentation techniques to the initial dataset using the following procedures: - In addition to the designated “initial state” of the adsorption process, where the adsorbate positioned 6.5 Å above the supported single metal atom, five intermediate images were

interpolated. These images were distributed between the initial and final states at a spacing of 0.5 Å, starting from the initial state side. - A diverse set of smearing techniques was employed to determine of partial occupancies f_{nk} , including the tetrahedron method [5] and the Gaussian method. For the Gaussian method, the smearing width was varied within the range of 0.01 eV to 0.1 eV. This careful selection of methods was made to guarantee reliable and consistent predictions of adsorption energies from the model, regardless of the smearing technique used.

The augmented dataset comprises 12,312 samples, with adsorption energies having a standard deviation of 1.8117 eV and a variance of 3.2821 eV₂. Twenty percent of these samples were allocated to the validation set. Throughout the training process, a batch size of 64 was employed to ensure a balanced learning dynamic.

3.8 eDOS occlusion experiments

Supplementary Figure 26 visually illustrates the eDOS occlusion experiment methodology. To maintain consistent shapes, zero-padding was applied to the input eDOS arrays. Focusing on understanding the influence of metals on adsorption behavior, a masker with dimensions [width, 1, 1] was employed along the metal channel to eliminate cross-orbital interactions. Here, “width” denotes the masker width, and detailed explanations for determining the width are provided in Supplementary section II.5. Through recursive application of these maskers, variations in predicted adsorption energies from the CNN model were recorded, generating an occlusion array.

3.9 eDOS shifting experiments

Supplementary Figure 35 illustrates the implemented eDOS shifting experiment protocol. In this study, the initial electronic density of states underwent controlled shifting along the energy axis. This protocol ranges from -1 eV to 1 eV, with a step length of 0.005 eV per image. To maintain a uniform energy window, each image underwent cropping and padding procedures. The resulted output arrays took the form of [400, 1] arrays for simultaneous orbital shifting and [400, 9] arrays for individual orbital shifting. The energy range for shifting was chosen to induce a moderate disturbance to adsorption energy.

3.10 Chemical bond analysis and real-space wavefunction visualization

COHP analysis was performed using the Local-Orbital Basis Suite Towards Electronic-Structure Reconstruction (LOBSTER) package [11, 33, 46, 43, 15] version 4.1.0,

with the GGA-PBE wavefunctions fitted by S. Maintz [33, 44]. A Gaussian smearing for energy integration was employed with a broadening width of 0.05 eV. The quantification of bonding strength between the single metal atom and the substrate was achieved through the summation of interactions with neighboring atoms within a range of 0.5 Å to 5.0 Å from the single metal atom. Orbitals of interest were confirmed through band-structure analysis, and real-space wavefunctions were subsequently visualized using VASPKIT [65] and VESTA [45].

3.11 Machine learning and data analysis environment

The CNN model was implemented using TensorFlow [1], and hyperparameter optimization was conducted using the Hyperband [41] algorithm via KerasTuner [50]. For a more detailed overview of our machine learning setup and data analysis environment, please refer to Supplementary section III.

A Code and Data Availability

Essential source code and data required to replicate the study’s results—including VASP input files, structure files of SACs, eDOS arrays and the pretrained CNN model—are available on GitHub repository at <https://github.com/DanielYang59/cnn4dos>, and can be provided by the corresponding authors upon request. Due to their substantial size in terabytes, the complete source data (complete VASP output files and such) is not currently hosted on publicly available repositories, but can be obtained from the corresponding authors upon request.

B Acknowledgements

We acknowledge funding support from the Australian Research Council (FT160100281, FT180100387, DP200103568, DP230101625). The QUT eResearch Office provided computational resources and services used in this work. This research was undertaken with the assistance of resources and services from the National Computational Infrastructure (NCI), supported by the Australian Government. It was also supported by resources provided by the Pawsey Supercomputing Research Centre with funding from the Australian Government and the Government of Western Australia. Insights into deep learning methodologies were contributed by Mr. Yanwei Guan from Chongqing University and Mr. Zhipeng He from Assoc. Prof. Chun Ouyang’s team at QUT. The machine learning and data analysis implementation benefited from resources provided by the GitHub, TensorFlow and Stack Overflow communities. Dr. Ryky Nelson from RWTH Aachen University offered valuable guidance on Crystal Orbital Hamilton Population analysis.

C Author Contributions

H.Y. performed DFT calculations, implemented Python code for machine learning methodologies and data analysis, and drafted and refined the manuscript. J.Z. engaged in valuable discussions on DFT calculations. Q.W. provided advice on the computer code revisions. B.L. provided guidance on DFT calculations and offered research supervision. W.L. facilitated resource acquisition and offered research supervision. Z.S. initiated the research concept, contributed to manuscript revisions, and supervised the overall research. T.L. guided DFT calculations and data analysis, offering continuous supervision throughout the research and manuscript drafting.

D Competing Interests

The authors declare no competing interests in relation to this research.

Supporting Information for:
Convolutional Neural Networks and Volcano Plots:
Screening and Prediction of Two-Dimensional Single-Atom
Catalysts for CO₂ Reduction Reactions

I Additional details on DFT calculations

I.1 Catalyst models

Representative structures for each substrate are depicted in Figure 7 through Figure 12. For the adsorption process, the initial state is defined by positioning the optimized adsorbates at a distance of 6.5 Å from the single-metal atoms supported on the substrate, oriented along the z-axis.

The periodic table shows the following color coding for investigated elements:

- Blue cells: Transition metals (Sc, Ti, V, Cr, Mn, Fe, Co, Ni, Cu, Zn, Ru, Rh, Pd, Ag, Cd, Hf, Ta, W, Re, Os, Ir, Pt, Au, Hg, Rf, Db, Sg, Bh, Hs, Mt, Ds, Rg, Cn, Nh, Fl, Mc, Lv, Ts).
- Purple cells: Metalloids (Ge, As, Se, Br, Sb, Te, I, Xe).
- Orange cells: Other metals (Al, Si, P, S, O, F, Cl, Ar, Tl, Pb, Bi, Po, At, Rn, Og).

Figure 6: Periodic table of investigated metals. Periodic table highlighting investigated elements: transition metals in blue, metalloids in purple, and other metals in orange.

I.2 CO₂RR pathways

In this study, we explored three reaction pathways that have been previously documented in the literature [16, 47, 53], as depicted in Figure 13. The adsorption configuration of the *CHO intermediate is pivotal in each of these pathways for determining the reaction mechanism in the CO₂RR process. We calculated the energies associated with the *CHO intermediate for catalysts supported on g-C₃N₄, nitrogen-doped graphene, and dual-vacancy graphene—under each mechanism. These calculations are summarized in section I.2. Our results indicate that Pathway 1 is the most energetically favorable for most catalysts we investigated. Therefore, to streamline our analysis, we focused exclusively on Mechanism 1 across all catalysts examined.

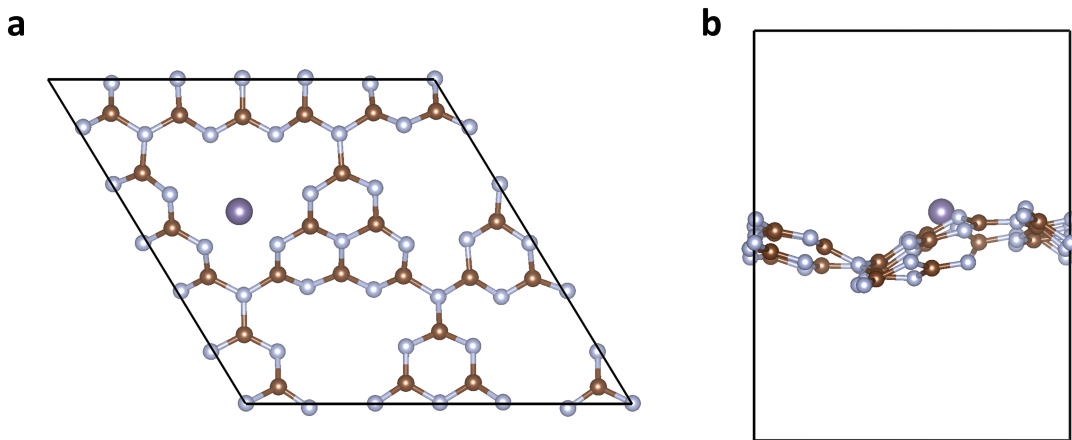


Figure 7: Structure of single germanium atom supported on graphitic nitride. (a) View along the z-axis and (b) view along the x-axis of the $\text{Ge@g-C}_3\text{N}_4$ structure. In the illustrations, silver spheres represent N atoms, brown spheres signify C atoms, and purple sphere indicates Ge atom.

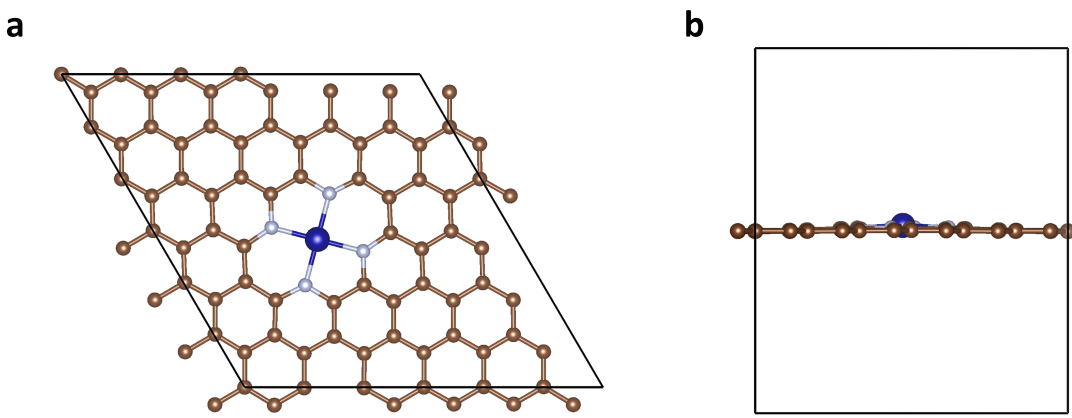


Figure 8: Structure of single chromium atom supported on nitrogen-doped graphene. (a) View along the z-axis and (b) view along the x-axis of the $\text{Cr@nitrogen-doped-graphene}$ structure. In the illustrations, silver spheres represent N atoms, brown spheres signify C atoms, and indigo sphere indicates Cr atom.

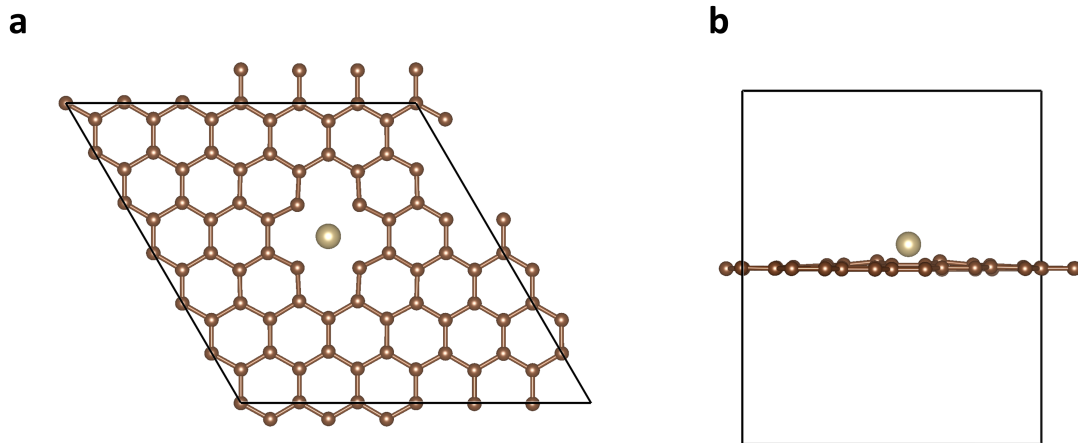


Figure 9: Structure of single osmium atom supported on graphene with dual-vacancy. (a) View along the z-axis and (b) view along the x-axis of the Os@graphene-with-dual-vacancy structure. In the illustrations, brown spheres signify C atoms, and light yellow sphere indicates Os atom.

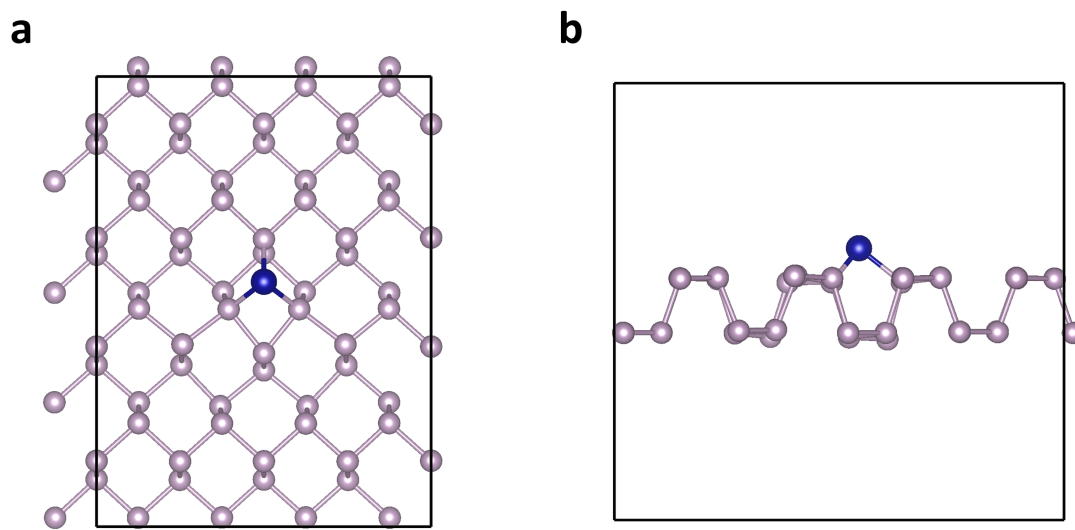


Figure 10: Structure of single chromium atom supported on black phosphorous. (a) View along the z-axis and (b) view along the x-axis of the Cr@black phosphorous structure. In the illustrations, light purple spheres represent P atoms, and indigo sphere indicates Cr atom.

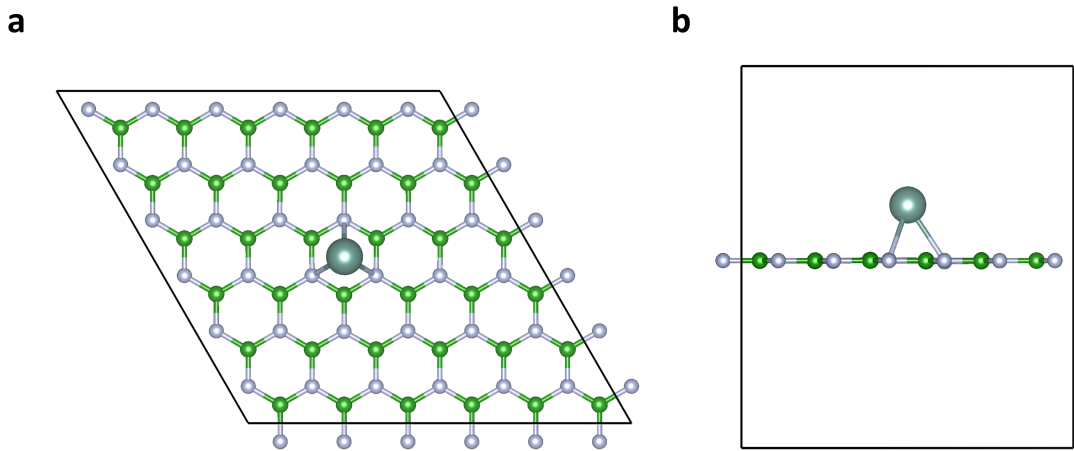


Figure 11: Structure of single yttrium atom supported on boron nitride. (a) View along the z-axis and (b) view along the x-axis of the Y@boron-nitride structure. In the illustrations, silver spheres represent N atoms, green spheres signify B atoms, and light green sphere indicates Y atom.

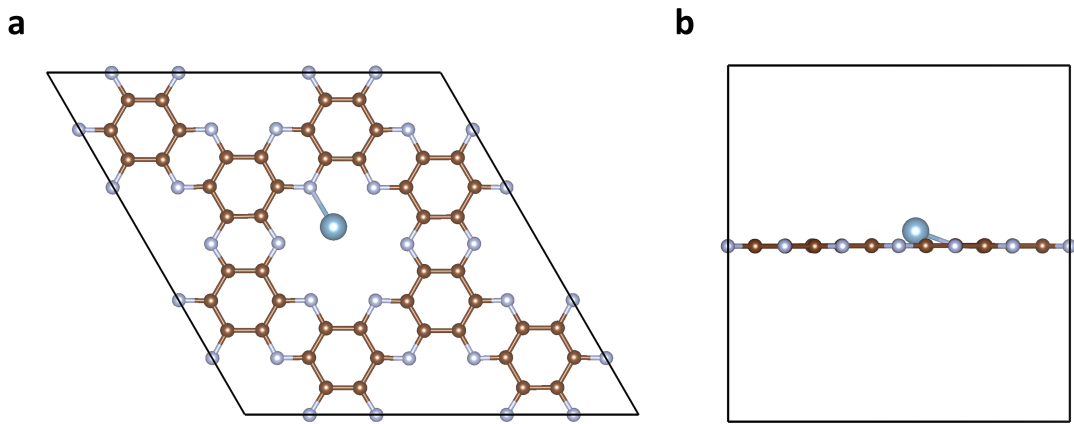
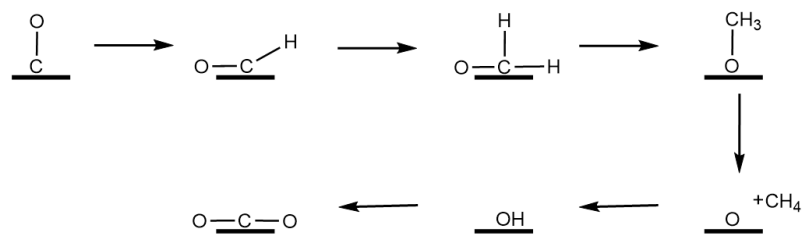
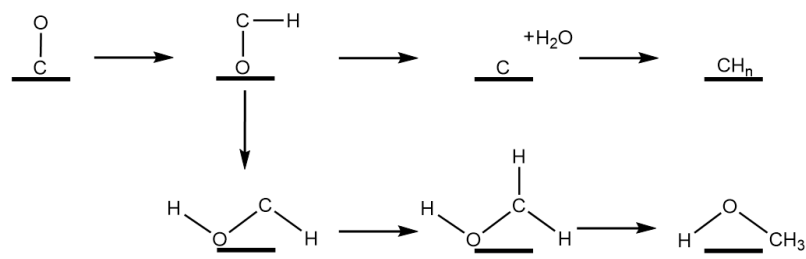


Figure 12: Structure of single aluminum atom supported on C₂N. (a) View along the z-axis and (b) view along the x-axis of the Al@C₂N structure. In the illustrations, silver spheres represent N atoms, brown spheres signify C atoms, and blue sphere indicates Al atom.

(1)



(2)



(3)

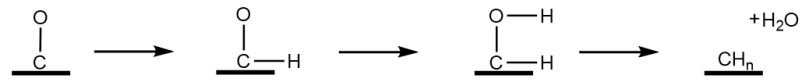


Figure 13: Three investigated CO₂RR pathways [16, 47, 53] investigated in this work.

Table 1: DFT-calculated energies in eV for protonated *CO intermediate for three investigated CO₂RR pathways.

Metal	g-C ₃ N ₄			nitrogen-doped graphene			graphene with dual-vacancy		
	Pathway-1	Pathway-2	Pathway-3	Pathway-1	Pathway-2	Pathway-3	Pathway-1	Pathway-2	Pathway-3
Al	-499.3494	-497.8343	-499.3005	-670.3489	-668.5142	-670.3093	-667.2538	-666.6725	-667.2665
Co	-502.5946	-501.1257	-502.6139	-672.8847	-670.8013	-672.9020	-671.6284	-670.4388	-671.3827
Cr	-505.6012	-504.2022	-505.6029	-675.3126	-674.1640	-675.3480	-673.4283	-672.1919	-673.3818
Cu	-495.8913	-493.6853	-495.8820	-666.9894	-664.9810	-666.9705	-666.9876	-664.7684	-667.1395
Fe	-501.3325	-499.3969	-501.3221	-673.8242	-672.0887	-673.8478	-672.7810	-671.5694	-672.4960
Ga	-498.2365	-496.3967	-498.2912	-667.3963	-665.4677	-667.3482	-665.7780	-664.8573	-665.8030
Ge	-500.2052	-497.9780	-500.2156	-668.1785	-666.3484	-668.1463	-667.7387	-665.7394	-667.7324
Mn	-502.6355	-500.8006	-502.6294	-674.6848	-672.9574	-674.7030	-673.2243	-672.6495	-673.2361
Ni	-500.4085	-498.5165	-500.3985	-670.0979	-667.9544	-670.0832	-670.1619	-668.3684	-670.1756
Sc	-503.4428	-501.6129	-503.4437	-673.9590	-671.7624	-673.3818	-670.0841	-668.1044	-669.6050
Ti	-503.7848	-502.6148	-503.8033	-675.1006	-673.2417	-674.6257	-672.7127	-670.6787	-672.2491
V	-503.6115	-502.6188	-503.5956	-675.0533	-674.0394	-675.0136	-673.1855	-671.5382	-673.1583
Zn	-493.9854	-491.5010	-493.9743	-664.9935	-663.0932	-664.9758	-663.7735	-661.8097	-663.7959
Ag	-494.4055	-492.4511	-494.3905	-664.6322	-662.9060	-664.6353	-664.3972	-662.3588	-665.0570
Cd	-493.3084	-491.1781	-493.2951	-663.8832	-661.6272	-663.8653	-661.8518	-659.9601	-661.8631
In	-498.5272	-496.6593	-498.5908	-666.3968	-663.7707	-666.3845	-663.6532	-661.5581	-663.6913
Mo	-504.5248	-503.3763	-504.5148	-675.3472	-674.7118	-675.4389	-674.7186	-672.9335	-674.7397
Nb	-505.3967	-504.7113	-505.3982	-676.0492	-674.1997	-675.4107	-674.6606	-672.8268	-674.5488
Pd	-500.0370	-498.3310	-500.0455	-669.0243	-667.0759	-669.0205	-669.1169	-667.3223	-669.1119
Rh	-499.2225	-497.3162	-499.2170	-672.7920	-670.7853	-672.8099	-671.4286	-670.3036	-671.4181
Ru	-503.9986	-502.1908	-503.9640	-674.0273	-672.4060	-674.0339	-672.9956	-672.1332	-672.9909
Sb	-497.3836	-495.1348	-497.3442	-666.7198	-664.9611	-666.7190	-666.8632	-664.8131	-666.8670
Sn	-499.4952	-497.2007	-499.1116	-667.1459	-665.3835	-667.0999	-665.9821	-663.8277	-665.9755
Tc	-503.0602	-501.1754	-503.0532	-674.4342	-673.8164	-674.4559	-674.0615	-672.9747	-674.0738
Y	-503.9232	-502.0670	-503.8988	-673.7620	-671.6132	-673.2241	-669.4633	-668.0403	-669.5030
Zr	-505.2907	-503.9148	-505.1817	-675.6874	-673.5456	-675.0519	-673.1694	-671.1993	-672.8072
Au	-497.0784	-495.1720	-497.0175	-665.1479	-663.3239	-665.1370	-666.4185	-664.2892	-666.5182
Bi	-496.9946	-494.7679	-496.9934	-665.9563	-664.2409	-666.0512	-665.0896	-663.2974	-665.0887
Hf	-506.4837	-504.9734	-506.4777	-677.3077	-675.1797	-676.6502	-674.7209	-672.6650	-674.2149
Hg	-491.0035	-488.7951	-490.9728	-661.2458	-659.2406	-661.2398	-661.7192	-659.8398	-661.7300
Ir	-503.0227	-501.1368	-503.0217	-673.9926	-672.0068	-674.0087	-673.5129	-672.6725	-673.4975
Os	-504.7648	-502.9878	-504.8105	-675.2098	-673.6653	-675.2235	-674.9483	-674.1970	-674.9223
Pb	-499.1183	-497.1173	-499.0544	-666.4446	-664.6897	-666.4625	-664.0200	-662.2222	-664.0123
Pt	-499.3356	-497.5110	-499.3215	-670.3996	-668.2412	-670.4147	-671.1408	-669.2725	-671.1370
Re	-504.1830	-502.4735	-504.1746	-675.7670	-675.0715	-675.7486	-675.8701	-674.9245	-675.8233
Ta	-506.6180	-505.7793	-506.6241	-677.7222	-675.9907	-677.0911	-676.4371	-674.5434	-676.4262
Tl	-497.9559	-496.1578	-497.9382	-664.5047	-662.7051	-664.5051	-662.6279	-660.6086	-662.6317
W	-505.8134	-504.9085	-505.8030	-676.5304	-676.1384	-676.9965	-676.7669	-675.4895	-676.7356

Note: Energies of the most stable configurations are highlighted in bold.

I.3 DFT energies and energy corrections

Table 2: Free energies at 298.15 K for isolated species.

Species	Free Energy (eV)
CO ₂	-23.3140
CO	-15.3336
CH ₄	-23.4639
H ₂	-6.9315
H ₂ O	-14.3239
COOH	-24.3963
CHO	-17.0983
CH ₂ O	-22.1607
OCH ₃	-24.5075
O	-1.9007
OH	-7.7303

Note: VASPKIT [65] was employed to calculate free energies.

I.4 Correlation analysis of adsorption energies

Figure 14 presents a Pearson correlation map that illustrates the relationships between the adsorption energies of various intermediates. This analysis encompasses all six substrates under consideration. The mean Pearson correlation coefficient is 0.6023 with a variance of 0.0109, signifying a robust correlation between the adsorption energies of different intermediates, accompanied by low variability.

I.5 The scaling relation scheme and the hybrid scaling relation

In line with the scaling relation framework proposed by Abild-Pedersen et al. [2], and later applied to the CO₂ reduction to methane process by Peterson & Nørskov [54], adsorbates in the CO₂RR process can be categorized into C-centered or O-centered species. In each group, a representative species is designated as the “descriptor”, allowing approximating the adsorption energies of other species within the same group using scaling relations. The following equations capture this relationship:

Table 3: Free energy corrections at 298.15 K for adsorbed intermediates.

Species	Free energy correction (eV)
*CO ₂	0.0864
*COOH	0.3693
*CO	0.0111
*CHO	0.2716
*CH ₂ O	0.5595
*OCH ₃	0.8738
*O	-0.0193
*OH	0.1993
*H	0.1533

Note: Free energy corrections were obtained by averaging the DFT-computed corrections, which include zero-point energy and entropy, across three substrates: g-C₃N₄, nitrogen-doped graphene, and dual-vacancy graphene.

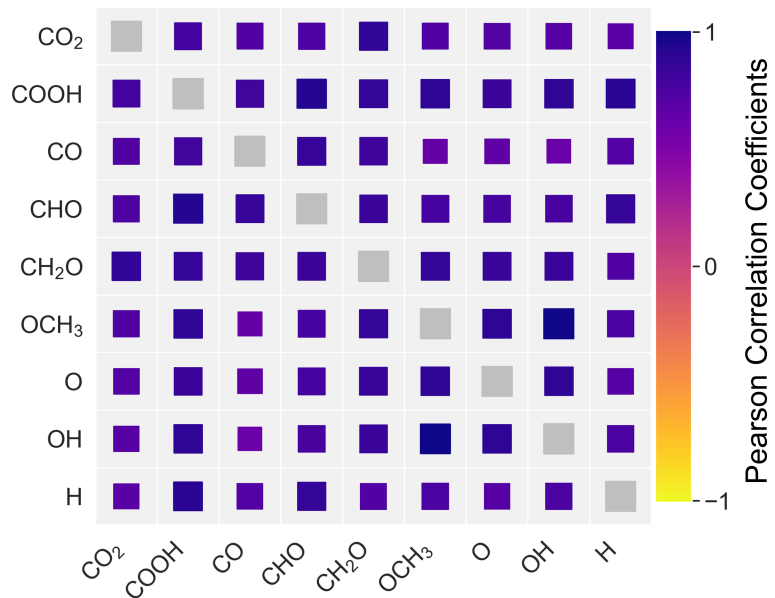


Figure 14: Pearson correlation map for adsorption energies of various adsorbates for all six substrates.

Table 4: DFT calculated final state energies in eV for adsorbates supported on g-C₃N₄.

Metal	*CO ₂	*COOH	*CO	*CHO	*CH ₂ O	*OCH ₃	*O	*OH	*H
Al	-481.2292	-504.7972	-508.6897	-496.4490	-500.7640	-503.7935	-509.9998	-488.6623	-485.4855
Co	-483.2039	-507.0765	-510.0453	-500.1329	-503.9316	-507.0552	-510.9052	-489.9487	-486.6194
Cr	-486.7813	-509.9599	-513.3962	-502.1493	-505.7125	-509.8851	-514.1702	-493.7457	-489.9202
Cu	-477.5955	-502.5914	-505.9613	-495.6511	-498.0502	-502.4590	-506.2829	-484.3166	-481.9683
Fe	-482.0576	-507.1508	-510.2918	-500.1101	-502.1626	-506.0115	-511.2543	-490.0116	-486.4067
Ga	-480.8854	-503.9317	-506.4938	-495.7379	-498.7813	-503.1345	-507.5029	-486.1702	-483.4575
Ge	-481.5807	-504.6467	-508.4204	-496.4421	-500.5712	-504.0218	-509.4116	-488.4168	-485.2680
Mn	-483.7690	-508.5410	-511.6514	-500.6279	-502.6739	-508.6433	-512.8569	-491.2239	-488.1082
Ni	-482.0061	-505.1988	-508.4173	-498.5054	-501.0040	-504.8945	-508.6266	-487.3684	-484.8272
Sc	-483.9963	-509.3147	-512.9882	-501.4505	-505.2024	-509.4054	-514.5969	-493.4105	-489.2632
Ti	-484.2282	-509.6510	-512.8528	-502.0410	-505.3761	-509.9729	-514.0700	-493.6478	-489.2234
V	-484.1990	-508.6926	-512.3009	-501.6777	-504.4297	-509.3618	-513.4561	-493.8569	-488.9474
Zn	-475.2375	-500.3556	-504.4103	-492.4144	-496.5426	-499.4232	-504.6297	-482.6782	-481.0438
Ag	-476.7049	-501.6430	-504.5861	-493.9138	-496.7220	-500.9477	-504.5408	-482.6604	-481.2659
Cd	-475.1288	-500.1854	-503.4108	-491.8954	-495.6486	-499.4959	-503.6209	-483.3427	-479.8278
In	-481.1330	-504.1653	-506.4422	-496.0016	-498.6643	-503.3286	-507.3780	-485.6281	-483.1445
Mo	-484.2892	-509.4263	-512.9103	-503.0025	-505.5534	-509.6730	-513.0136	-493.5700	-489.4994
Nb	-485.4055	-510.7952	-514.0380	-503.5663	-506.3671	-511.1572	-514.7845	-495.5118	-490.2111
Pd	-481.5399	-504.7593	-508.5173	-498.0817	-501.1620	-504.0892	-508.1976	-486.1551	-483.9553
Rh	-479.8884	-505.2422	-508.6754	-498.7129	-501.4594	-504.5254	-508.9536	-487.8771	-485.0738
Ru	-483.8526	-507.5120	-511.5881	-500.6857	-504.1497	-506.8934	-510.9524	-490.6690	-488.0169
Sb	-478.5169	-502.9708	-506.5211	-494.8740	-498.9453	-502.5347	-507.2111	-486.4448	-483.4418
Sn	-481.4238	-504.4677	-507.8470	-496.2883	-499.9258	-503.6685	-508.8152	-487.6963	-484.6351
Tc	-482.7091	-507.9652	-512.1064	-501.9896	-504.6034	-508.3486	-511.4777	-492.0381	-488.0897
Y	-484.6612	-509.8564	-513.6851	-501.9522	-505.8238	-509.8344	-515.2400	-493.4038	-489.6506
Zr	-485.4694	-511.1852	-514.3901	-503.1958	-506.9346	-511.5864	-515.6720	-496.3037	-490.4785
Au	-479.1941	-502.3245	-506.9013	-495.6782	-499.0711	-501.6877	-506.5462	-484.6198	-483.6909
Bi	-478.2695	-502.8490	-506.2055	-494.6965	-498.5557	-502.3398	-506.7999	-485.7536	-483.1348
Hf	-486.5155	-512.4535	-515.5965	-504.3393	-508.1599	-512.8332	-517.2187	-496.4195	-491.7486
Hg	-472.8730	-500.0491	-502.1889	-491.7544	-494.1224	-499.2181	-501.8365	-480.3761	-479.2046
Ir	-483.7878	-507.2024	-510.6763	-500.2051	-503.2948	-506.5209	-509.8509	-490.9790	-487.3503
Os	-484.9279	-508.6427	-512.5954	-501.8541	-505.2080	-507.8334	-511.8734	-491.0155	-489.0898
Pb	-481.3587	-504.4450	-507.5634	-496.2379	-499.6114	-503.5822	-508.1698	-486.8476	-484.2646
Pt	-481.1676	-504.3670	-508.2170	-499.0073	-500.9446	-504.2695	-508.1465	-487.3508	-484.6644
Re	-483.6421	-508.9474	-512.8388	-502.8952	-505.3651	-509.1168	-512.6374	-493.0621	-489.2811
Ta	-486.3299	-512.1371	-515.1895	-504.6585	-507.5888	-512.5295	-516.0165	-497.0134	-490.5695
Tl	-480.7357	-503.7632	-505.9937	-495.5894	-497.7724	-503.0564	-506.7919	-484.0732	-482.3846
W	-485.2596	-510.8145	-514.28	-504.2714	-506.7988	-511.0643	-514.2358	-494.4330	-490.6506

Table 5: DFT calculated final state energies in eV for adsorbates supported on nitrogen-doped graphene.

Metal	*CO ₂	*COOH	*CO	*CHO	*CH ₂ O	*OCH ₃	*O	*OH	*H
Al	-652.7589	-675.7997	-679.7595	-668.0296	-671.7596	-676.2161	-681.1311	-658.7849	-656.4702
Co	-654.3280	-677.5394	-681.2518	-670.0860	-673.9208	-676.7761	-680.7219	-659.1714	-657.8777
Cr	-657.0479	-680.2074	-683.7982	-673.0760	-676.1859	-679.4701	-684.5295	-664.7306	-660.4141
Cu	-650.2181	-673.3928	-675.5873	-665.2174	-668.0662	-672.5797	-675.7047	-653.5770	-652.1010
Fe	-655.4034	-678.5897	-682.1186	-671.9101	-674.7438	-677.8515	-682.1216	-661.5422	-658.7383
Ga	-649.9563	-672.9807	-676.9763	-664.9727	-669.0739	-672.8536	-677.7169	-655.5345	-653.9243
Ge	-651.0391	-674.1655	-677.2582	-665.9255	-669.5282	-673.3438	-678.1585	-657.4964	-654.3444
Mn	-656.5635	-679.7128	-683.1092	-672.6753	-675.6877	-679.0710	-683.3898	-663.1584	-659.7760
Ni	-653.1461	-676.3270	-678.5166	-668.1448	-671.1502	-675.5454	-678.5411	-656.3929	-655.1238
Sc	-655.2274	-678.9985	-682.8810	-670.9489	-674.9850	-679.1986	-684.3192	-662.2442	-659.0243
Ti	-655.5937	-680.2412	-683.5514	-671.9689	-675.9724	-680.4589	-685.1366	-665.2871	-659.7132
V	-656.0751	-680.2584	-683.5739	-672.6281	-676.0229	-680.5926	-684.9400	-665.6038	-659.9017
Zn	-648.2316	-671.3824	-674.1973	-663.2623	-666.3990	-670.5613	-674.5436	-652.2900	-650.9227
Ag	-646.9759	-670.2666	-673.2766	-663.1058	-665.7601	-669.7801	-673.0113	-651.0760	-649.9287
Cd	-646.1687	-669.2620	-672.8043	-661.4439	-664.9473	-668.8180	-672.9588	-650.7684	-649.7670
In	-648.6726	-671.7218	-675.3788	-663.4885	-667.5183	-670.7536	-675.8630	-653.8535	-652.4757
Mo	-655.7944	-680.2966	-683.6262	-672.7667	-676.3955	-680.6291	-684.8234	-665.8138	-659.8169
Nb	-656.0277	-680.8814	-684.2662	-672.5576	-676.9139	-681.4203	-685.7720	-666.2363	-660.3734
Pd	-652.2091	-675.3967	-677.2760	-667.1855	-669.8609	-674.6033	-677.3498	-655.1080	-654.0027
Rh	-653.6928	-676.9529	-680.9755	-669.5137	-673.6394	-676.2879	-680.2104	-658.6953	-657.6908
Ru	-654.5425	-678.2124	-681.9561	-672.0589	-674.6177	-678.0945	-681.9008	-661.3838	-658.6572
Sb	-649.9262	-672.9182	-675.6457	-664.7128	-667.9159	-672.0849	-675.8420	-655.1699	-652.4240
Sn	-650.5072	-673.6118	-675.7767	-665.3842	-668.0544	-672.7597	-676.5046	-655.8947	-652.9261
Tc	-655.4025	-679.3044	-682.7454	-672.5785	-676.3294	-679.4840	-683.3209	-664.2323	-659.2703
Y	-655.2660	-679.0430	-682.7571	-670.8208	-674.7780	-679.0775	-684.1210	-661.8034	-658.8885
Zr	-655.9118	-680.6859	-684.1920	-672.1497	-676.4014	-680.7930	-685.7940	-665.4878	-660.4163
Au	-648.3344	-671.3969	-673.1469	-663.1955	-665.5964	-670.5800	-673.6092	-651.2436	-649.7275
Bi	-649.1484	-672.1225	-675.1630	-663.9594	-667.2981	-671.4617	-675.6926	-654.7684	-651.8907
Hf	-657.3364	-682.3019	-685.8119	-673.6603	-678.0090	-682.4001	-687.4607	-666.9550	-662.0651
Hg	-644.7368	-667.9224	-671.2200	-659.6906	-663.5208	-667.0466	-670.9016	-648.8944	-648.3755
Ir	-654.8564	-678.1079	-682.2865	-670.9826	-674.9484	-677.4097	-681.3088	-660.1543	-658.9895
Os	-655.6722	-679.5364	-683.3240	-673.4289	-675.9254	-679.4423	-683.1300	-663.0791	-659.9901
Pb	-649.8843	-672.9588	-674.5856	-664.7553	-667.1174	-672.0886	-675.8823	-653.6827	-651.5940
Pt	-653.3281	-676.5221	-678.6094	-668.2951	-671.2463	-675.7317	-678.4334	-656.4419	-655.4733
Re	-656.3492	-680.7664	-683.9596	-673.9732	-676.5164	-681.0627	-684.8096	-665.9526	-660.5620
Ta	-657.1988	-682.6048	-685.8231	-674.1666	-678.5029	-682.9709	-687.2294	-667.7321	-661.8794
Tl	-648.1346	-671.1831	-673.2953	-662.9610	-665.6240	-670.3512	-673.4567	-651.7909	-650.4750
W	-657.0204	-682.0186	-685.3735	-674.3843	-678.2483	-682.4377	-686.3613	-667.4547	-661.5686

Table 6: DFT calculated final state energies in eV for adsorbates supported on graphene with dual-vacancy.

Metal	*CO ₂	*COOH	*CO	*CHO	*CH ₂ O	*OCH ₃	*O	*OH	*H
Al	-650.3496	-673.3468	-676.2273	-665.6303	-668.4112	-672.5763	-677.4453	-655.0864	-653.0166
Co	-652.5157	-675.5864	-679.3861	-669.0614	-672.8955	-675.8508	-679.5268	-658.7929	-655.9377
Cr	-655.0421	-678.1256	-681.8470	-671.1282	-674.2868	-679.1554	-683.4111	-663.3554	-658.4913
Cu	-649.8187	-672.9161	-674.9327	-664.8190	-669.0819	-672.1515	-674.7438	-652.8789	-653.6953
Fe	-653.7964	-677.0127	-680.3412	-670.0219	-673.9525	-676.7631	-681.1346	-660.9239	-656.9759
Ga	-649.0340	-672.0433	-674.9630	-663.8505	-667.2101	-671.2541	-675.5229	-653.2086	-651.8693
Ge	-651.0133	-674.2532	-677.2272	-666.0554	-669.5660	-673.4485	-677.8152	-655.7843	-654.2731
Mn	-654.8183	-678.0584	-681.5834	-670.9593	-674.0994	-677.9260	-682.6048	-662.5702	-658.1064
Ni	-651.5295	-674.6692	-677.8941	-667.2937	-670.7325	-673.9392	-677.5204	-656.1026	-655.6559
Sc	-652.1630	-675.5777	-678.6101	-667.5024	-670.7255	-675.4361	-680.0287	-658.0834	-654.6913
Ti	-654.2548	-677.9326	-681.1516	-670.0780	-673.2830	-677.9113	-682.6933	-661.1957	-657.4040
V	-654.6939	-678.0200	-681.8606	-670.8517	-674.2298	-679.2097	-683.4928	-663.1639	-658.4619
Zn	-646.9805	-670.1676	-672.2508	-662.0849	-664.7199	-669.3791	-672.6028	-650.3134	-648.8961
Ag	-647.4840	-670.5954	-672.4765	-662.3757	-665.1014	-669.8199	-672.2893	-650.2207	-651.5223
Cd	-645.2038	-668.3897	-670.2685	-660.2502	-662.7479	-667.5994	-670.6023	-648.2958	-646.9658
In	-646.8189	-669.9379	-673.1820	-661.7351	-665.3833	-669.1524	-673.5557	-651.3730	-650.2004
Mo	-656.2058	-679.7202	-683.2424	-672.3832	-675.6459	-679.9903	-684.8002	-664.6331	-659.9673
Nb	-656.1010	-679.4842	-683.3623	-672.0587	-675.6683	-679.5996	-684.8935	-664.2634	-659.9617
Pd	-650.5405	-673.6524	-677.0119	-666.0816	-669.7529	-672.9394	-676.5341	-655.1586	-654.8764
Rh	-652.7998	-675.8992	-679.6974	-669.1468	-672.2062	-676.2142	-679.9592	-659.4214	-656.7388
Ru	-654.8166	-678.0140	-681.6090	-671.1415	-674.0502	-677.9828	-682.4415	-662.4653	-658.2092
Sb	-649.9882	-673.0639	-675.9906	-664.8414	-668.3621	-672.2685	-676.6274	-655.1055	-653.1345
Sn	-648.5997	-671.7246	-675.2765	-663.7120	-667.5399	-670.8850	-675.8484	-653.8138	-652.4041
Tc	-655.8173	-679.2476	-682.6345	-672.1709	-675.0076	-679.2729	-683.7569	-664.1434	-659.2908
Y	-652.1517	-675.4891	-678.6682	-667.4644	-670.6934	-675.1478	-680.0013	-658.3045	-654.7163
Zr	-654.8760	-678.4572	-681.6839	-670.6090	-673.8291	-678.4537	-683.1390	-661.4741	-657.9892
Au	-649.3963	-672.5116	-674.3660	-664.2836	-667.3357	-671.7273	-674.1359	-652.0358	-653.1138
Bi	-648.8651	-672.0004	-673.7920	-663.7934	-666.2170	-671.1801	-674.0672	-652.8628	-650.9149
Hf	-656.1155	-679.7805	-683.2130	-671.9925	-675.3123	-679.9256	-684.7502	-662.8630	-659.4860
Hg	-645.0948	-668.2801	-669.9749	-660.1062	-662.5696	-667.4822	-670.2672	-647.8582	-646.7652
Ir	-654.4999	-677.8310	-681.7312	-671.1936	-674.7821	-678.1749	-681.9532	-661.9662	-658.5262
Os	-656.3635	-679.8433	-683.4557	-673.1036	-675.9479	-679.6710	-684.4704	-664.7281	-660.0873
Pb	-647.8007	-670.9491	-673.2996	-662.7392	-665.6502	-670.1373	-673.5969	-651.6692	-650.4432
Pt	-652.4961	-675.6092	-678.9183	-668.2053	-671.6867	-674.8876	-678.4355	-657.4936	-656.2759
Re	-657.2440	-681.0777	-684.5183	-673.9603	-676.8950	-681.2383	-685.8328	-666.1615	-661.2885
Ta	-657.4068	-681.0711	-685.1062	-673.5947	-677.3738	-681.6985	-686.7561	-666.0327	-661.7361
Tl	-645.7286	-668.8734	-671.7205	-660.7259	-664.0001	-668.1110	-672.0305	-649.7198	-648.7563
W	-657.5901	-681.6722	-685.1010	-674.1028	-677.7828	-682.4493	-686.6385	-666.9364	-661.8641

Table 7: Zero-point energies in eV for relaxed adsorbates supported on g-C₃N₄ at 298.15 K.

Metal	*CO ₂	*COOH	*CO	*CHO	*CH ₂ O	*OCH ₃	*O	*OH	*H
Al	0.2905	0.6130	0.1743	0.4606	0.7456	1.0974	0.0629	0.3521	0.1925
Co	0.3038	0.5895	0.2051	0.4186	0.6269	1.0663	0.0571	0.3248	0.1507
Cr	0.3140	0.5964	0.1640	0.4374	0.7725	1.0779	0.0670	0.3286	0.1626
Cu	0.3157	0.6016	0.2045	0.4498	0.7797	1.0751	0.0494	0.3332	0.1577
Fe	0.3088	0.5859	0.1931	0.4437	0.7720	1.0726	0.0599	0.3326	0.1550
Ga	0.3102	0.6131	0.1448	0.4665	0.7186	1.0680	0.0608	0.3202	0.1813
Ge	0.3091	0.6069	0.1396	0.4540	0.7269	1.0881	0.0581	0.3506	0.1904
Mn	0.3022	0.5876	0.1733	0.4333	0.7637	1.0622	0.0687	0.3219	0.1432
Ni	0.3023	0.5934	0.2074	0.4546	0.7662	1.0623	0.0542	0.3313	0.1611
Sc	0.2880	0.6039	0.1771	0.4544	0.7473	1.0806	0.0657	0.3156	0.1480
Ti	0.3044	0.6088	0.1889	0.4664	0.7863	1.0862	0.0796	0.3417	0.1590
V	0.3081	0.6005	0.2031	0.4408	0.7868	1.0882	0.0792	0.3388	0.1660
Zn	0.3243	0.6080	0.1729	0.4601	0.7277	1.0832	0.0514	0.3468	0.1726
Ag	0.3167	0.5993	0.1815	0.4457	0.7264	1.0590	0.0390	0.3304	0.1576
Cd	0.3242	0.6007	0.1533	0.4502	0.7292	1.0604	0.0983	0.3322	0.1439
In	0.3116	0.5687	0.1399	0.4025	0.7158	1.0551	0.0523	0.3315	0.1141
Mo	0.3109	0.6071	0.2163	0.4441	0.7970	1.0825	0.0765	0.3312	0.1851
Nb	0.3101	0.5971	0.2013	0.4340	0.7960	1.0908	0.0798	0.3329	0.1598
Pd	0.3148	0.6091	0.1996	0.4778	0.7402	1.0777	0.0525	0.3425	0.1508
Rh	0.3064	0.6180	0.2215	0.4654	0.7649	1.0844	0.0615	0.3643	0.1946
Ru	0.3060	0.6201	0.2104	0.4668	0.7761	1.0800	0.0663	0.3421	0.2026
Sb	0.3050	0.6244	0.1461	0.4696	0.7473	1.1052	0.0689	0.3676	0.2043
Sn	0.3115	0.5941	0.1441	0.4373	0.7202	1.0761	0.0591	0.3397	0.1601
Tc	0.3170	0.6102	0.2178	0.4543	0.7890	1.0807	0.0698	0.3442	0.2008
Y	0.2768	0.5949	0.1712	0.4467	0.7278	1.0780	0.0573	0.3206	0.1349
Zr	0.2939	0.6068	0.1888	0.4631	0.7737	1.0875	0.0744	0.3155	0.1592
Au	0.3123	0.6245	0.2147	0.4761	0.7312	1.0845	0.0527	0.3432	0.2066
Bi	0.3076	0.6148	0.1485	0.4612	0.7392	1.0935	0.0611	0.3554	0.1893
Hf	0.2928	0.6104	0.1880	0.4658	0.7769	1.0954	0.0765	0.3218	0.1728
Hg	0.3220	0.6221	0.1486	0.4707	0.7338	1.0809	0.0541	0.3469	0.1924
Ir	0.3127	0.6311	0.2271	0.4818	0.7530	1.0740	0.1084	0.3314	0.2142
Os	0.3122	0.6260	0.2258	0.4796	0.7531	1.0911	0.0670	0.3501	0.2154
Pb	0.3152	0.5834	0.1401	0.4239	0.7113	1.0486	0.0513	0.3043	0.1352
Pt	0.3144	0.6361	0.2225	0.4908	0.7569	1.0921	0.0603	0.3672	0.2058
Re	0.3171	0.6175	0.2213	0.4665	0.8021	1.0985	0.0780	0.3597	0.2032
Ta	0.3099	0.5977	0.2000	0.4414	0.7993	1.0880	0.0847	0.3410	0.1780
Tl	0.3114	0.5614	0.1389	0.3494	0.7105	1.0410	0.0246	0.3210	0.0951
W	0.3146	0.6059	0.2160	0.4456	0.8033	1.0886	0.0725	0.3387	0.1834

Table 8: Entropy corrections ($-T \cdot S$) in eV for relaxed adsorbates supported on g-C₃N₄ at 298.15 K.

Metal	*CO ₂	*COOH	*CO	*CHO	*CH ₂ O	*OCH ₃	*O	*OH	*H
Al	-0.2195	-0.2476	-0.1874	-0.1939	-0.2359	-0.1759	-0.0894	-0.1010	-0.0124
Co	-0.2359	-0.2665	-0.1544	-0.1572	-0.1755	-0.2095	-0.1078	-0.1510	-0.0341
Cr	-0.1862	-0.2605	-0.2075	-0.2069	-0.1478	-0.1733	-0.0790	-0.1437	-0.0221
Cu	-0.3098	-0.2403	-0.1655	-0.1803	-0.1647	-0.2378	-0.0977	-0.1375	-0.0297
Fe	-0.2184	-0.2028	-0.1676	-0.1797	-0.1742	-0.2640	-0.0815	-0.1285	-0.0215
Ga	-0.2602	-0.2558	-0.2291	-0.1881	-0.1252	-0.2576	-0.0897	-0.1441	-0.0182
Ge	-0.1978	-0.2423	-0.1635	-0.1802	-0.2104	-0.2364	-0.1178	-0.1052	-0.0087
Mn	-0.2142	-0.2678	-0.1863	-0.2059	-0.1788	-0.2752	-0.0808	-0.1425	-0.0261
Ni	-0.2460	-0.1948	-0.1592	-0.1224	-0.1275	-0.2506	-0.0997	-0.1384	-0.0224
Sc	-0.2227	-0.2369	-0.1843	-0.1667	-0.1817	-0.2035	-0.0728	-0.1416	-0.0226
Ti	-0.1978	-0.2263	-0.1685	-0.1389	-0.1414	-0.1795	-0.0578	-0.1013	-0.0195
V	-0.2603	-0.2511	-0.1452	-0.2028	-0.1360	-0.2374	-0.0612	-0.1082	-0.0186
Zn	-0.2928	-0.2543	-0.1909	-0.1959	-0.2202	-0.2331	-0.0910	-0.1185	-0.0228
Ag	-0.2458	-0.2428	-0.1910	-0.1890	-0.3097	-0.2421	-0.1060	-0.1392	-0.0276
Cd	-0.2961	-0.2561	-0.2368	-0.2023	-0.2076	-0.2630	-0.0270	-0.1408	-0.0337
In	-0.1978	-0.2895	-0.1071	-0.1840	-0.1338	-0.2826	-0.1011	-0.1386	-0.0405
Mo	-0.1912	-0.2310	-0.1310	-0.1680	-0.1269	-0.2228	-0.0641	-0.1496	-0.0155
Nb	-0.1896	-0.2540	-0.1460	-0.1924	-0.1290	-0.2147	-0.0575	-0.1177	-0.0261
Pd	-0.2405	-0.2385	-0.1649	-0.1740	-0.2538	-0.2201	-0.0900	-0.1143	-0.0518
Rh	-0.2408	-0.2385	-0.1355	-0.1734	-0.1853	-0.2247	-0.0863	-0.0866	-0.0222
Ru	-0.2197	-0.2304	-0.1450	-0.1769	-0.1655	-0.1574	-0.0832	-0.1294	-0.0138
Sb	-0.2354	-0.2277	-0.1320	-0.1793	-0.2211	-0.1961	-0.0616	-0.0808	-0.0090
Sn	-0.2606	-0.2544	-0.2227	-0.2021	-0.3045	-0.2568	-0.0787	-0.1171	-0.0160
Tc	-0.1875	-0.2373	-0.1347	-0.1733	-0.1485	-0.2301	-0.0697	-0.1007	-0.0121
Y	-0.2557	-0.2528	-0.1929	-0.1886	-0.2130	-0.2081	-0.0824	-0.1393	-0.0285
Zr	-0.2083	-0.2325	-0.1624	-0.1459	-0.1574	-0.2014	-0.0640	-0.1556	-0.0208
Au	-0.1901	-0.2267	-0.1484	-0.1846	-0.2939	-0.2307	-0.0857	-0.1271	-0.0138
Bi	-0.2366	-0.2392	-0.1915	-0.1899	-0.2361	-0.1986	-0.0683	-0.0934	-0.0100
Hf	-0.2043	-0.2219	-0.1618	-0.1418	-0.1489	-0.1981	-0.0610	-0.1414	-0.0163
Hg	-0.2980	-0.2371	-0.2812	-0.1995	-0.3039	-0.2465	-0.0878	-0.1245	-0.0175
Ir	-0.2097	-0.2290	-0.1261	-0.1803	-0.1913	-0.2221	-0.0377	-0.1379	-0.0159
Os	-0.1795	-0.2235	-0.1294	-0.1519	-0.1609	-0.2027	-0.0680	-0.1093	-0.0124
Pb	-0.2546	-0.2691	-0.1666	-0.2165	-0.2641	-0.2520	-0.1007	-0.1097	-0.0257
Pt	-0.2411	-0.2029	-0.1496	-0.1593	-0.2009	-0.2246	-0.0950	-0.0937	-0.0137
Re	-0.1869	-0.2262	-0.1293	-0.1697	-0.1266	-0.2165	-0.0644	-0.0953	-0.0146
Ta	-0.1872	-0.2532	-0.1523	-0.1847	-0.1265	-0.1798	-0.0535	-0.1040	-0.0177
Tl	-0.2599	-0.2833	-0.1807	-0.1538	-0.2422	-0.1501	-0.0126	-0.1338	-0.0533
W	-0.1791	-0.2368	-0.1335	-0.1723	-0.1225	-0.2253	-0.0673	-0.1180	-0.0201

Table 9: Zero-point energies in eV for relaxed adsorbates supported on nitrogen-doped graphene at 298.15 K.

Metal	*CO ₂	*COOH	*CO	*CHO	*CH ₂ O	*OCH ₃	*O	*OH	*H
Al	0.3093	0.6024	0.1683	0.4395	0.7509	1.0855	0.0552	0.3401	0.1864
Co	0.3140	0.6247	0.2044	0.4787	0.7345	1.0615	0.0606	0.3315	0.2006
Cr	0.3108	0.5983	0.2007	0.4410	0.7211	1.0824	0.0828	0.3253	0.1625
Cu	0.3145	0.5943	0.1460	0.4377	0.7196	1.0160	0.0407	0.3104	0.1523
Fe	0.3117	0.6148	0.2195	0.4634	0.7877	1.0678	0.0703	0.3163	0.1858
Ga	0.3129	0.6080	0.1561	0.4537	0.7495	1.0826	0.0573	0.3420	0.1897
Ge	0.3131	0.6206	0.1402	0.4629	0.7281	1.1014	0.0686	0.3538	0.2110
Mn	0.3120	0.6111	0.2128	0.4601	0.8078	1.0640	0.0793	0.3148	0.2040
Ni	0.3110	0.6059	0.1485	0.4602	0.7283	1.0467	0.0402	0.3168	0.1620
Sc	0.2741	0.5910	0.1620	0.4456	0.7019	1.0758	0.0575	0.3166	0.1338
Ti	0.2920	0.6020	0.1781	0.4525	0.7593	1.0831	0.0731	0.2981	0.1481
V	0.2984	0.6055	0.1865	0.4609	0.7756	1.0843	0.0786	0.3171	0.1525
Zn	0.3143	0.5928	0.1554	0.4357	0.7116	1.0521	0.0394	0.3248	0.1640
Ag	0.3127	0.5862	0.1862	0.4307	0.7518	1.0419	0.0356	0.3231	0.1308
Cd	0.3055	0.5910	0.1518	0.4402	0.7312	1.0524	0.0366	0.3189	0.1483
In	0.3096	0.5986	0.1414	0.4477	0.7152	1.0724	0.0437	0.3300	0.1609
Mo	0.2949	0.6111	0.1914	0.4728	0.7806	1.0887	0.0795	0.3253	0.1500
Nb	0.2946	0.5996	0.1767	0.4601	0.7874	1.0896	0.0742	0.3048	0.1515
Pd	0.3122	0.5993	0.1444	0.4490	0.7303	1.0342	0.0300	0.3047	0.1558
Rh	0.3115	0.6288	0.1969	0.4826	0.7388	1.0867	0.0602	0.3453	0.2025
Ru	0.3152	0.6122	0.2180	0.4569	0.7918	1.0947	0.0698	0.3483	0.1873
Sb	0.3115	0.5874	0.1397	0.4349	0.7184	1.0467	0.0646	0.3351	0.1752
Sn	0.3112	0.6002	0.1400	0.4367	0.7239	1.0836	0.0568	0.3359	0.1710
Tc	0.3053	0.6110	0.2105	0.4251	0.7934	1.0870	0.0807	0.3496	0.1741
Y	0.2709	0.5835	0.1580	0.4307	0.7059	1.0703	0.0500	0.3200	0.1226
Zr	0.2719	0.5963	0.1723	0.4430	0.7327	1.0846	0.0669	0.3176	0.1472
Au	0.3137	0.5480	0.1442	0.3577	0.7209	0.9864	0.0174	0.2881	0.1027
Bi	0.3111	0.5778	0.1378	0.4190	0.7133	1.0475	0.0550	0.3241	0.1533
Hf	0.2699	0.6002	0.1714	0.4452	0.7372	1.0904	0.0687	0.3242	0.1569
Hg	0.3113	0.6082	0.1397	0.4569	0.7258	1.0720	0.0412	0.3304	0.1625
Ir	0.3132	0.6309	0.2106	0.4856	0.7390	1.0888	0.0626	0.3456	0.2022
Os	0.3156	0.6148	0.2179	0.4592	0.7971	1.0984	0.0768	0.3463	0.1812
Pb	0.3116	0.5352	0.1385	0.3677	0.7147	1.0532	0.0474	0.3172	0.1302
Pt	0.3139	0.6134	0.1439	0.4671	0.7359	1.0406	0.0482	0.3114	0.1736
Re	0.3035	0.6045	0.2095	0.4566	0.7995	1.0957	0.0846	0.3493	0.1818
Ta	0.2751	0.6019	0.1869	0.4630	0.7724	1.0937	0.0751	0.3060	0.1669
Tl	0.3131	0.5988	0.1402	0.4439	0.7193	1.0169	0.0573	0.3244	0.1506
W	0.2889	0.6117	0.1927	0.4777	0.7852	1.0941	0.0810	0.3273	0.1832

Table 10: Entropy corrections ($-T \cdot S$) in eV for relaxed adsorbates supported on nitrogen-doped graphene at 298.15 K.

Metal	*CO ₂	*COOH	*CO	*CHO	*CH ₂ O	*OCH ₃	*O	*OH	*H
Al	-0.1981	-0.2564	-0.1979	-0.1424	-0.2051	-0.1839	-0.0794	-0.1211	-0.0113
Co	-0.2358	-0.2213	-0.1589	-0.1584	-0.2025	-0.2223	-0.0701	-0.0817	-0.0123
Cr	-0.2593	-0.1973	-0.1568	-0.2037	-0.2291	-0.1679	-0.0569	-0.0875	-0.0228
Cu	-0.2457	-0.2636	-0.2132	-0.2040	-0.1267	-0.2137	-0.1188	-0.1711	-0.0226
Fe	-0.1936	-0.2385	-0.1356	-0.1758	-0.1985	-0.1910	-0.0647	-0.0892	-0.0172
Ga	-0.2565	-0.1937	-0.1600	-0.2025	-0.2139	-0.1766	-0.0727	-0.1269	-0.0126
Ge	-0.2469	-0.2413	-0.1027	-0.1937	-0.1687	-0.1551	-0.0690	-0.1091	-0.0080
Mn	-0.1929	-0.2402	-0.1409	-0.1736	-0.1949	-0.2011	-0.0563	-0.1631	-0.0160
Ni	-0.1239	-0.2440	-0.2027	-0.1785	-0.2318	-0.1792	-0.0929	-0.1520	-0.0170
Sc	-0.1938	-0.2647	-0.1418	-0.2024	-0.2291	-0.2139	-0.0790	-0.1516	-0.0293
Ti	-0.2093	-0.2423	-0.1798	-0.1640	-0.1765	-0.1433	-0.0692	-0.1462	-0.0262
V	-0.2112	-0.2373	-0.1734	-0.1578	-0.1642	-0.0767	-0.0621	-0.1522	-0.0273
Zn	-0.2567	-0.2001	-0.2491	-0.2135	-0.1581	-0.1396	-0.1091	-0.1668	-0.0211
Ag	-0.2600	-0.2035	-0.1802	-0.2231	-0.1723	-0.1531	-0.1293	-0.1487	-0.0596
Cd	-0.2615	-0.2042	-0.1827	-0.2185	-0.2727	-0.2094	-0.1192	-0.1850	-0.0320
In	-0.1886	-0.2021	-0.1593	-0.2221	-0.1949	-0.2061	-0.1158	-0.1603	-0.0238
Mo	-0.2049	-0.2075	-0.1659	-0.1327	-0.1650	-0.2041	-0.0605	-0.1258	-0.0437
Nb	-0.2072	-0.2300	-0.1145	-0.1439	-0.1403	-0.2086	-0.0684	-0.1863	-0.0251
Pd	-0.1843	-0.2620	-0.1476	-0.2000	-0.1645	-0.2057	-0.1131	-0.1688	-0.0223
Rh	-0.2986	-0.2220	-0.1669	-0.1667	-0.1953	-0.1423	-0.0693	-0.1229	-0.0149
Ru	-0.1998	-0.1779	-0.1375	-0.1827	-0.1455	-0.2017	-0.0653	-0.1103	-0.0202
Sb	-0.1938	-0.1984	-0.1084	-0.2024	-0.1970	-0.0996	-0.0780	-0.1183	-0.0109
Sn	-0.1931	-0.2040	-0.1708	-0.2214	-0.1801	-0.2006	-0.0911	-0.1474	-0.0185
Tc	-0.2038	-0.2277	-0.1483	-0.1505	-0.1515	-0.1810	-0.0569	-0.1008	-0.0234
Y	-0.1994	-0.2704	-0.1507	-0.1605	-0.2919	-0.2162	-0.0981	-0.1548	-0.0344
Zr	-0.2233	-0.2608	-0.1845	-0.1849	-0.2016	-0.2144	-0.0776	-0.1500	-0.0242
Au	-0.1872	-0.1923	-0.2237	-0.1738	-0.1907	-0.2639	-0.1497	-0.1276	-0.0301
Bi	-0.1978	-0.2736	-0.1731	-0.1581	-0.2369	-0.0995	-0.0937	-0.1386	-0.0171
Hf	-0.2235	-0.2562	-0.1836	-0.1839	-0.1987	-0.2082	-0.0759	-0.1417	-0.0211
Hg	-0.1907	-0.1929	-0.1053	-0.0955	-0.1765	-0.2558	-0.1157	-0.1694	-0.0357
Ir	-0.2967	-0.2218	-0.1486	-0.1659	-0.2038	-0.2134	-0.0723	-0.1326	-0.0200
Os	-0.1948	-0.2462	-0.1422	-0.1945	-0.1448	-0.2046	-0.0598	-0.1205	-0.0322
Pb	-0.1979	-0.2320	-0.1108	-0.2414	-0.1437	-0.2639	-0.1126	-0.1465	-0.0238
Pt	-0.1770	-0.2479	-0.1481	-0.1915	-0.2820	-0.2030	-0.0791	-0.1666	-0.0228
Re	-0.1958	-0.2535	-0.1508	-0.1867	-0.1462	-0.2483	-0.0561	-0.1018	-0.0249
Ta	-0.2078	-0.2197	-0.1675	-0.1373	-0.1542	-0.2084	-0.0698	-0.1979	-0.0195
Tl	-0.2573	-0.2043	-0.1719	-0.2270	-0.1288	-0.2326	-0.0688	-0.1876	-0.0332
W	-0.2007	-0.2007	-0.1642	-0.1194	-0.1565	-0.2032	-0.0607	-0.1275	-0.0202

Table 11: Zero-point energies in eV for relaxed adsorbates supported on graphene with dual-vacancy at 298.15 K.

Metal	*CO ₂	*COOH	*CO	*CHO	*CH ₂ O	*OCH ₃	*O	*OH	*H
Al	0.3140	0.5988	0.1888	0.4386	0.7218	1.0769	0.0472	0.3366	0.1729
Co	0.3080	0.6179	0.2173	0.4899	0.7928	1.0616	0.0573	0.3458	0.1726
Cr	0.3318	0.5862	0.1957	0.4277	0.8826	1.0733	0.0792	0.3294	0.1560
Cu	0.3140	0.6023	0.1769	0.5229	0.7172	1.0131	0.0323	0.3298	0.2857
Fe	0.3177	0.6110	0.2083	0.5038	0.7828	1.0802	0.0776	0.3515	0.1987
Ga	0.3126	0.6056	0.1492	0.4494	0.7196	1.0788	0.0446	0.3370	0.1810
Ge	0.3138	0.6171	0.1471	0.4657	0.7196	1.0935	0.0540	0.3514	0.2028
Mn	0.3167	0.6141	0.2050	0.4803	0.8009	1.0809	0.0756	0.3411	0.1594
Ni	0.3134	0.6251	0.1942	0.4571	0.7230	1.0738	0.0496	0.3521	0.2877
Sc	0.3229	0.5874	0.1668	0.4367	0.7358	1.0673	0.0533	0.3129	0.1288
Ti	0.3240	0.6049	0.1749	0.4562	0.7202	1.0694	0.0670	0.3143	0.1559
V	0.2937	0.6042	0.1933	0.4593	0.8437	1.0745	0.0753	0.3319	0.1687
Zn	0.3123	0.5888	0.1564	0.4317	0.7111	1.0363	0.0324	0.3157	0.1363
Ag	0.3172	0.5984	0.1399	0.4312	0.7199	1.0034	0.0258	0.3141	0.2932
Cd	0.3120	0.5796	0.1487	0.4176	0.7144	1.0198	0.0278	0.3084	0.1280
In	0.3134	0.5973	0.1458	0.4443	0.7170	1.0666	0.0418	0.3236	0.1610
Mo	0.3052	0.5923	0.1942	0.4668	0.7718	1.0844	0.0745	0.3350	0.1755
Nb	0.2952	0.6071	0.1862	0.4605	0.7505	1.0749	0.0721	0.3274	0.1717
Pd	0.3151	0.6191	0.1872	0.4609	0.7187	1.0525	0.0397	0.3371	0.2963
Rh	0.2870	0.6096	0.2076	0.4297	0.7850	1.0628	0.0604	0.3590	0.2678
Ru	0.3000	0.6040	0.2097	0.4645	0.7812	1.0710	0.0790	0.3319	0.1758
Sb	0.3122	0.6143	0.1436	0.4604	0.7258	1.0938	0.0608	0.3481	0.1912
Sn	0.3132	0.6077	0.1493	0.4550	0.7182	1.0807	0.0517	0.3338	0.1770
Tc	0.3051	0.6025	0.2086	0.4585	0.7777	1.0690	0.0799	0.3285	0.2898
Y	0.3219	0.5847	0.1632	0.4299	0.7245	1.0646	0.0557	0.3182	0.1164
Zr	0.3213	0.5966	0.1669	0.4527	0.7200	1.0620	0.0568	0.3151	0.1510
Au	0.3172	0.5927	0.1448	0.4677	0.7261	0.9827	0.0291	0.2904	0.2898
Bi	0.3108	0.6062	0.1406	0.4521	0.7185	1.0309	0.0528	0.3289	0.1696
Hf	0.3241	0.5981	0.1713	0.4543	0.7236	1.0751	0.0586	0.3142	0.1550
Hg	0.3130	0.5763	0.1421	0.3959	0.7161	0.9951	0.0177	0.2917	0.1258
Ir	0.3054	0.6129	0.2147	0.4199	0.7939	1.0680	0.0712	0.3603	0.1863
Os	0.3033	0.6068	0.2155	0.4695	0.7674	1.0779	0.0823	0.3330	0.1401
Pb	0.3118	0.6044	0.1424	0.4518	0.7199	1.0740	0.0502	0.3250	0.1623
Pt	0.3124	0.6242	0.1985	0.4680	0.7263	1.0514	0.0477	0.3406	0.2725
Re	0.3033	0.6034	0.2108	0.4601	0.7864	1.0807	0.0780	0.3317	0.2191
Ta	0.2938	0.6078	0.1872	0.4601	0.7707	1.0754	0.0732	0.3243	0.1783
Tl	0.3091	0.5948	0.1424	0.4406	0.7123	1.0568	0.0342	0.3173	0.1569
W	0.3066	0.6062	0.1912	0.3984	0.8010	1.0777	0.0787	0.3333	0.1815

Table 12: Entropy corrections ($-T \cdot S$) in eV for relaxed adsorbates supported on graphene with dual-vacancy at 298.15 K.

Metal	*CO ₂	*COOH	*CO	*CHO	*CH ₂ O	*OCH ₃	*O	*OH	*H
Al	-0.2501	-0.2622	-0.1799	-0.2106	-0.3101	-0.2050	-0.0980	-0.1303	-0.0165
Co	-0.1962	-0.2352	-0.1529	-0.1520	-0.1515	-0.0821	-0.0427	-0.1165	-0.0376
Cr	-0.2178	-0.2281	-0.1603	-0.2297	-0.0849	-0.0961	-0.0623	-0.1200	-0.0250
Cu	-0.1907	-0.2528	-0.1276	-0.1239	-0.1974	-0.2279	-0.0711	-0.1357	-0.0044
Fe	-0.2328	-0.2473	-0.0848	-0.1300	-0.1611	-0.1248	-0.0629	-0.0996	-0.0292
Ga	-0.1842	-0.2577	-0.2003	-0.2061	-0.1912	-0.2332	-0.0956	-0.1395	-0.0145
Ge	-0.2491	-0.1850	-0.1442	-0.1942	-0.1974	-0.1522	-0.0886	-0.1119	-0.0101
Mn	-0.2384	-0.2493	-0.1559	-0.1654	-0.1993	-0.1304	-0.0599	-0.1090	-0.0275
Ni	-0.2497	-0.2279	-0.1683	-0.1836	-0.2402	-0.2254	-0.1159	-0.1027	-0.0021
Sc	-0.2252	-0.1996	-0.1449	-0.2023	-0.2586	-0.2259	-0.1128	-0.1670	-0.0322
Ti	-0.2137	-0.2297	-0.1918	-0.1703	-0.2184	-0.2455	-0.0745	-0.1598	-0.0186
V	-0.2319	-0.2441	-0.1693	-0.1713	-0.0933	-0.0952	-0.0673	-0.1171	-0.0164
Zn	-0.1971	-0.2071	-0.1798	-0.2147	-0.1577	-0.2074	-0.1203	-0.1637	-0.0293
Ag	-0.2465	-0.2579	-0.1696	-0.1739	-0.1930	-0.2345	-0.0117	-0.1000	-0.0038
Cd	-0.1963	-0.2145	-0.2124	-0.2350	-0.2120	-0.2341	-0.1338	-0.1754	-0.0354
In	-0.2567	-0.2013	-0.1464	-0.1558	-0.2003	-0.1995	-0.1043	-0.1065	-0.0228
Mo	-0.2106	-0.2086	-0.1656	-0.1746	-0.1628	-0.2038	-0.0668	-0.1129	-0.0144
Nb	-0.2307	-0.2394	-0.1752	-0.1660	-0.1679	-0.1668	-0.0688	-0.1288	-0.0138
Pd	-0.3134	-0.2362	-0.1751	-0.1707	-0.1779	-0.0819	-0.0677	-0.1222	-0.0039
Rh	-0.2128	-0.2468	-0.1542	-0.1986	-0.1595	-0.0720	-0.0949	-0.0933	-0.0021
Ru	-0.2275	-0.2613	-0.1426	-0.1760	-0.1693	-0.0786	-0.0577	-0.1332	-0.0175
Sb	-0.1891	-0.1940	-0.2266	-0.1526	-0.2398	-0.2284	-0.0788	-0.1157	-0.0132
Sn	-0.2529	-0.1968	-0.2028	-0.2165	-0.1898	-0.1845	-0.0886	-0.1568	-0.0170
Tc	-0.2158	-0.2603	-0.1459	-0.1731	-0.1578	-0.0973	-0.0574	-0.1222	-0.0647
Y	-0.2962	-0.2657	-0.1496	-0.2075	-0.2598	-0.2231	-0.1096	-0.1662	-0.0384
Zr	-0.1548	-0.2417	-0.1360	-0.1770	-0.2745	-0.2015	-0.0919	-0.1551	-0.0185
Au	-0.2413	-0.2076	-0.2877	-0.1138	-0.2448	-0.2634	-0.0095	-0.1447	-0.0041
Bi	-0.1970	-0.2006	-0.2337	-0.1648	-0.1315	-0.2394	-0.0927	-0.1399	-0.0183
Hf	-0.2728	-0.2398	-0.1920	-0.1784	-0.2711	-0.3070	-0.0834	-0.1620	-0.0186
Hg	-0.1953	-0.2848	-0.1710	-0.1987	-0.2065	-0.1285	-0.1491	-0.1469	-0.0370
Ir	-0.2144	-0.1796	-0.1476	-0.1609	-0.1474	-0.0751	-0.0699	-0.0953	-0.0258
Os	-0.2163	-0.2409	-0.1420	-0.1599	-0.1776	-0.0816	-0.0565	-0.1218	-0.0724
Pb	-0.1964	-0.2001	-0.2339	-0.1644	-0.1894	-0.1890	-0.0888	-0.1086	-0.0227
Pt	-0.1825	-0.2340	-0.1657	-0.1759	-0.2307	-0.1921	-0.0612	-0.1216	-0.0022
Re	-0.2117	-0.2566	-0.1472	-0.1661	-0.1530	-0.1479	-0.0619	-0.1223	-0.0261
Ta	-0.2269	-0.2462	-0.1744	-0.1715	-0.1696	-0.1787	-0.0694	-0.1428	-0.0135
Tl	-0.1981	-0.2044	-0.2304	-0.2198	-0.2048	-0.2595	-0.1146	-0.1764	-0.0256
W	-0.2006	-0.2433	-0.1670	-0.1453	-0.1295	-0.1025	-0.0613	-0.1185	-0.0157

$$G_{\text{ads}}X = a_X \cdot G_{\text{ads}}\text{CO} + c_X \quad (\text{where } X = \text{COOH, CHO, CH}_2\text{O}) \quad (16)$$

$$G_{\text{ads}}Y = a_Y \cdot G_{\text{ads}}\text{OH} + c_Y \quad (\text{where } Y = \text{O, OCH}_3) \quad (17)$$

Here, CO and OH serve as descriptors for C-centered (X) and O-centered (Y) groups, respectively, and a_X, c_X, a_Y, c_Y are species-specific scaling parameters. The scaling relations simplify the adsorption energy landscape to a two-dimensional space, thereby enabling visualization.

However, it's crucial to note that in the CO₂RR process, most species are not solely C- or O-centered. Thus, it becomes advantageous to incorporate both types of species in the scaling relation. Building upon the hybrid scaling relation introduced in the main text, the free energy change (ΔG) for any given reaction step can be readily calculated using Equation (14) from the main text. Consider the generic reaction step:



The free energy change ΔG is defined as:

$$\Delta G = G({}^*\text{B}) - G({}^*\text{A}) - G(\text{H}^+) - G(\text{e}^-) \quad (19)$$

Focusing on any reaction step delineated by Equation (1) to Equation (8) in the main text, Equation (15) shows that limiting potential U_L at a specific external potential U is fully determined by the adsorption energies of two descriptors. For instance, for the reaction described by Equation (3):

$$\Delta G = G({}^*\text{COOH}) - G({}^*) - G(\text{CO}_2) - G(\text{H}^+) - G(\text{e}^-) \quad (20)$$

$$= G(\text{COOH}) + G({}^*) + G_{\text{ads}}\text{COOH} - G({}^*) - G(\text{CO}_2) - G(\text{H}^+) - G(\text{e}^-) \quad (21)$$

$$= G_{\text{ads}}\text{COOH} + G(\text{COOH}) - G(\text{CO}_2) - G(\text{H}^+) - G(\text{e}^-) \quad (22)$$

From adsorption energy linear relations, we have:

$$G_{\text{ads}}\text{COOH} = a_{\text{COOH}} \cdot G_{\text{ads}}\text{CO} + b_{\text{COOH}} \cdot G_{\text{ads}}\text{OH} + c_{\text{COOH}} \quad (23)$$

which then reduces Supplementary Equation (22) to:

$$\begin{aligned} \Delta G = & (a_{\text{COOH}} \cdot G_{\text{ads}}\text{CO} + b_{\text{COOH}} \cdot G_{\text{ads}}\text{OH}) + \\ & [c_{\text{COOH}} + G(\text{COOH}) - G(\text{CO}_2) - G(\text{H}^+) - G(\text{e}^-)] \end{aligned} \quad (24)$$

In this case, the first term depends solely on the descriptors, while the second term remains constant at a given potential U .

Table 13: Adsorption free energy scaling relation parameters determined by the hybrid descriptor method.

Adsorbate	a_Z	b_Z	c_Z
COOH	0.4032	0.5132	0.0899
CHO	0.5977	0.3664	-2.6763
CH ₂ O	0.5011	0.5011	-0.9806
OCH ₃	0.0532	1.0114	0.8489
O	0.3758	1.2580	0.0910
H	0.3164	0.3568	-0.6764

Note: a_Z , b_Z and c_Z correspond to coefficients for $G_{\text{ads}}\text{CO}$, $G_{\text{ads}}\text{OH}$ and constant terms, where Z stands for the adsorbed species of interest.

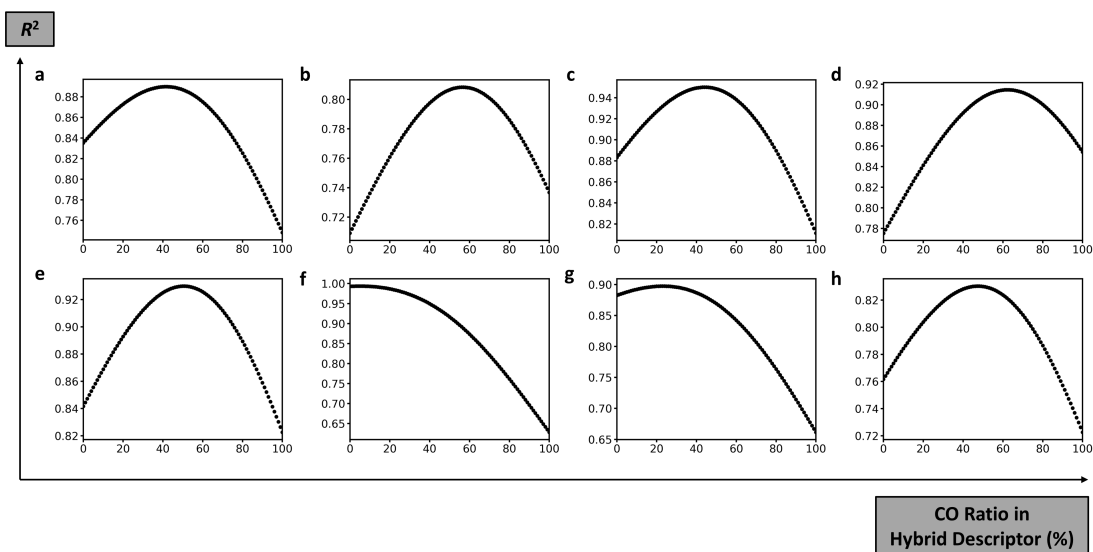


Figure 15: R^2 improvement from hybrid-descriptor method. Improvement in the coefficient of determination (R^2) with x-axis as CO ratio in CO/OH hybrid descriptors. (a) averaged R^2 and those of (b) CO₂, (c) COOH, (d) CHO, (e) CH₂O, (f) OCH₃, (g) O and (h) H are shown.

Table 14: Performance comparison of hybrid descriptor and single descriptor for linear scaling relations.

Adsorbate	Hybrid Descriptor R^2 (Optimal CO Ratio)	Single Descriptor R^2 Reference Species	R^2
CO ₂	0.8083 (57%)	0.7368 (CO)	0.0715
COOH	0.9500 (44%)	0.8113 (CO)	0.1387
CHO	0.9146 (62%)	0.8541 (CO)	0.0605
CH ₂ O	0.9299 (50%)	0.8226 (CO)	0.1073
OCH ₃	0.9936 (5%)	0.9929 (OH)	0.0007
O	0.8974 (23%)	0.8825 (OH)	0.0149
H	0.8303 (47%)	0.7617 (OH)	0.0686

I.6 Volcano plots

In addition to the selectivity volcano plot featured in the main text, we provide a comprehensive plot capturing all rate-determining steps for CO₂RR in Figure 16. A separate plot focusing on selectivity over HER is also presented in Figure 17.

I.7 Activity periodic tables

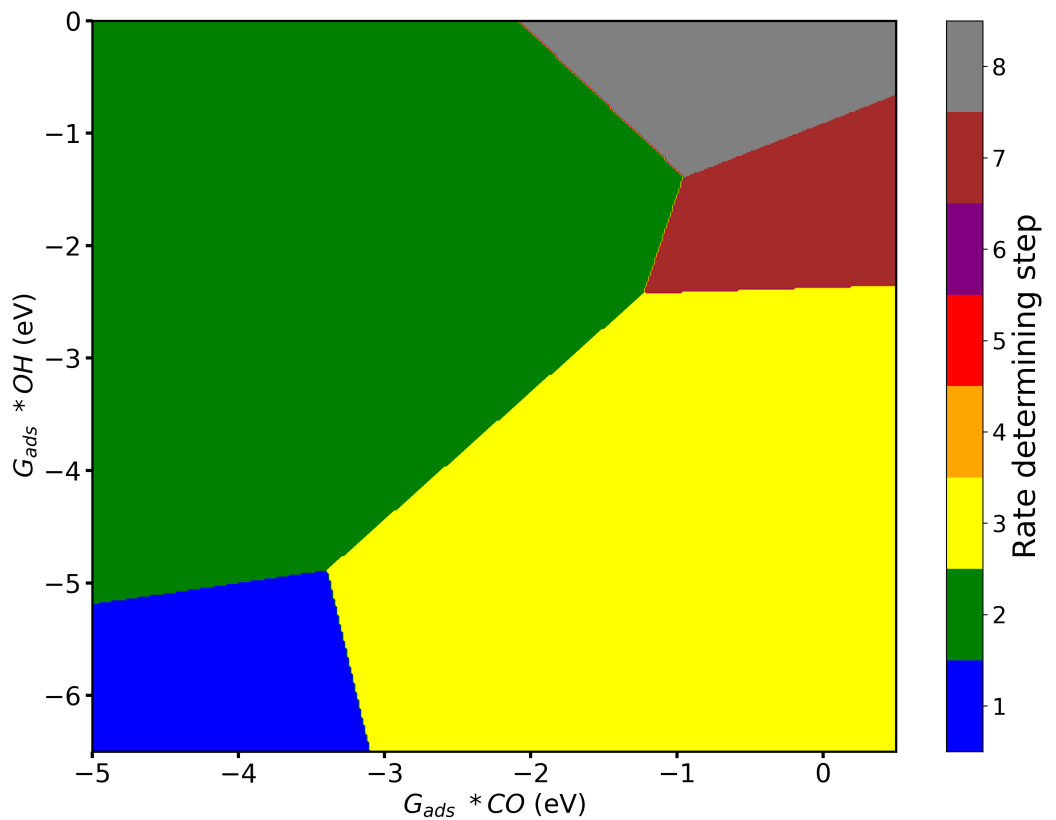


Figure 16: CO₂RR rate determining step volcano plot. This graph illustrates the rate-determining step associated with each region within the CO₂RR process.

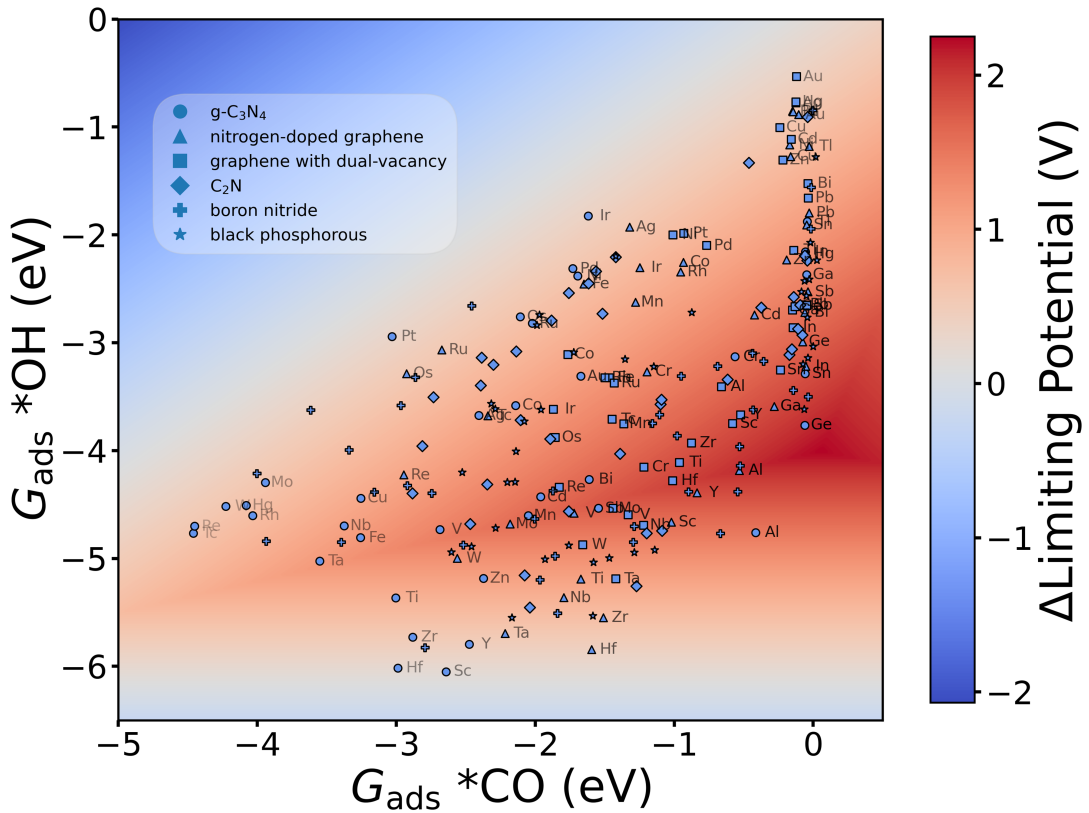


Figure 17: CO₂RR selectivity volcano plot. Selectivity volcano plot computed from linear scaling relations. In the plot, the circle, triangle, square, diamond, plus, and star symbols correspond to metals supported on g-C₃N₄, nitrogen-doped graphene, graphene with dual-vacancy, black phosphorous, BN, and C₂N, respectively.

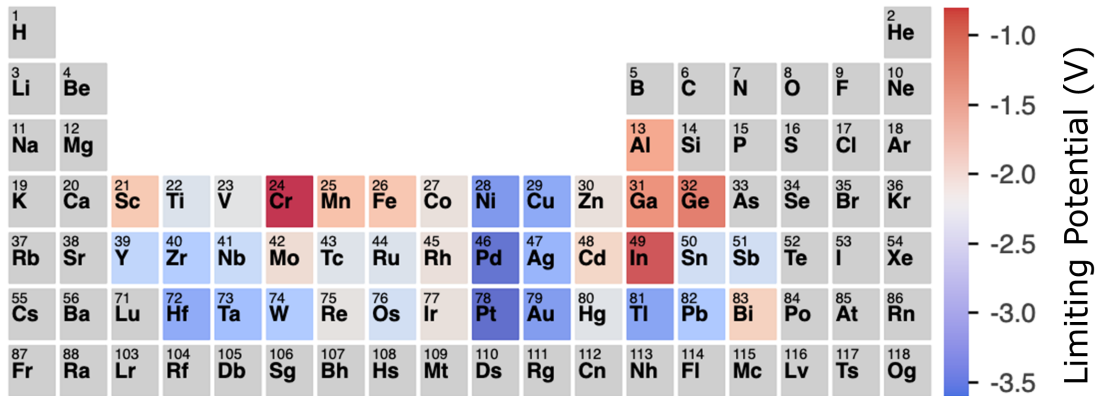


Figure 18: Limiting potential periodic table for nitrogen-doped graphene.

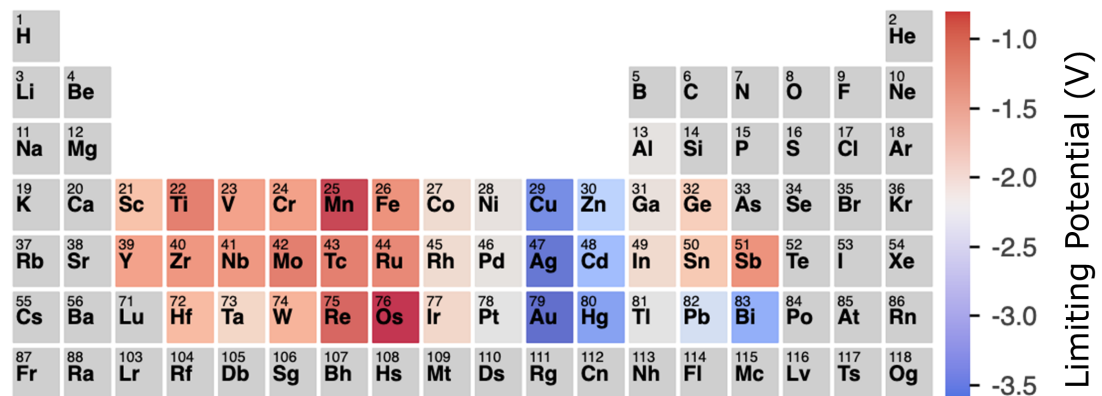


Figure 19: Limiting potential periodic table for graphene with dual-vacancy.

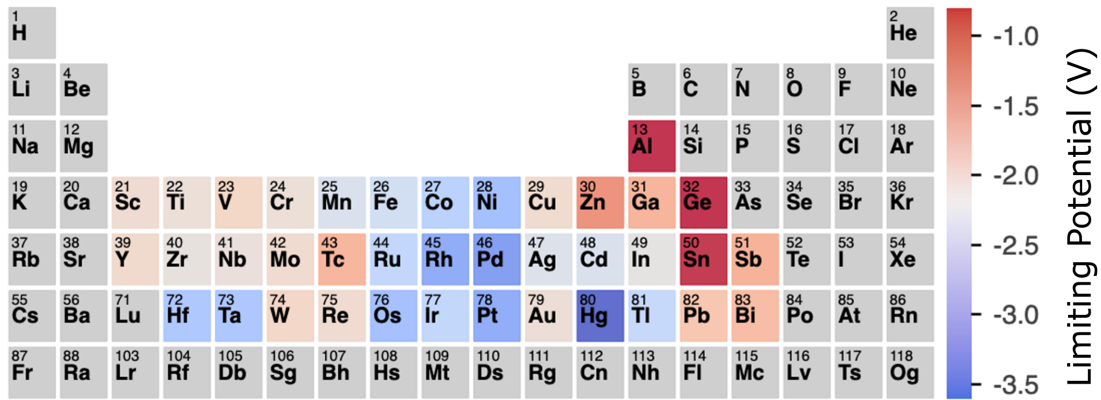


Figure 20: Limiting potential periodic table for black phosphorus.

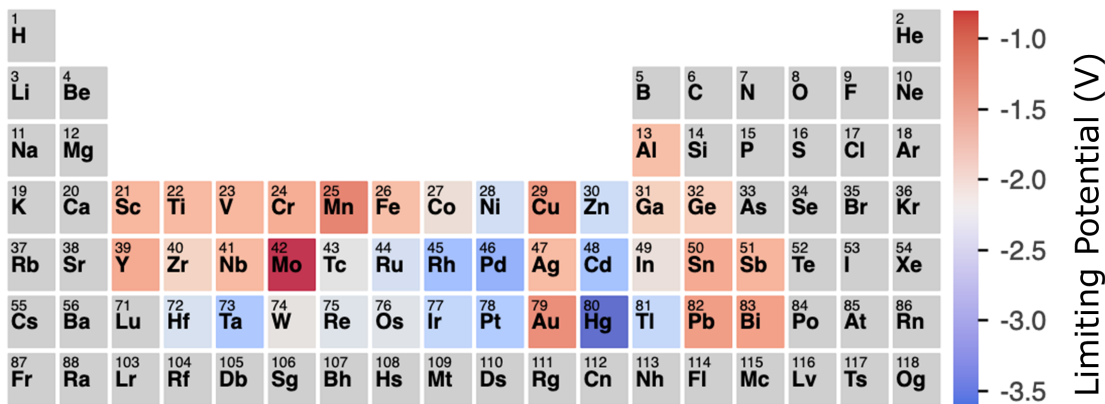


Figure 21: Limiting potential periodic table for boron nitride.

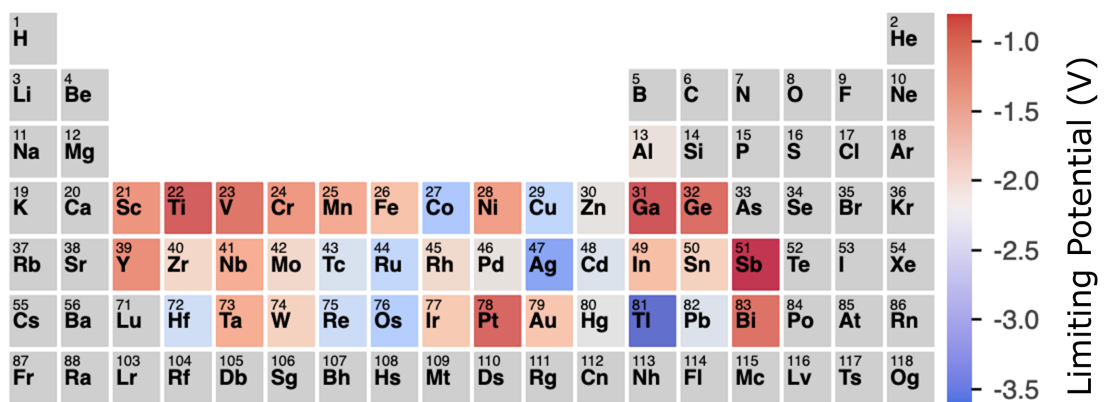


Figure 22: Limiting potential periodic table for monolayer C_2N .

II Additional details on machine learning method

II.1 d-band center and adsorption energy relations

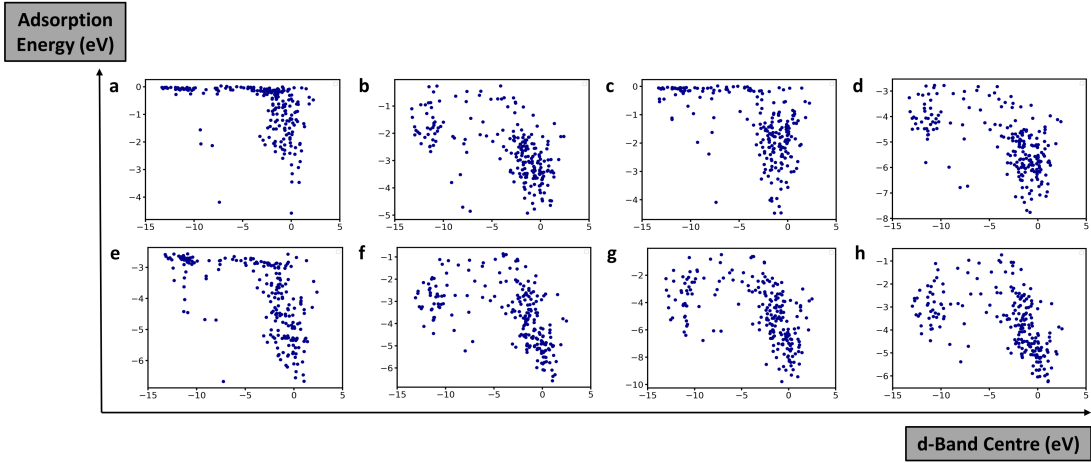


Figure 23: Scatter plot of d-Band Center and Adsorption Energy Relationships. This figure delineates the relationship between d-band center and adsorption energies for various species: (a) CO₂, (b) COOH, (c) CO, (d) CHO, (e) CH₂O, (f) OCH₃, (g) O, and (h) OH. Data from all six substrates investigated in this study are included.

II.2 Feature correlation analysis

Figure 24 displays the pairwise relationships between CO adsorption energy and its four most correlated descriptors: d-band center (spin-up) $\delta\epsilon_d \uparrow$, lattice parameter γ , vacuum level E_{vac} , and electronegativity on the Allen scale χ_{Allen} , identified by Kendall rank correlation analysis. section II.2 lists notations for elementary descriptors and electronic descriptors.

II.3 Input pipeline construction

The format of the 2D array for the eDOS is naturally well-suited for use as neural network inputs. In this study, the array adopts a shape of [numSamplings, numOrbitals, numChannels], as illustrated in Figure 25. Here, “numSamplings” represents the number of data points sampled across the energy spectrum, “numOrbitals” denotes the number of DOS orbitals, and “numChannels” indicates the number of atomic channels.

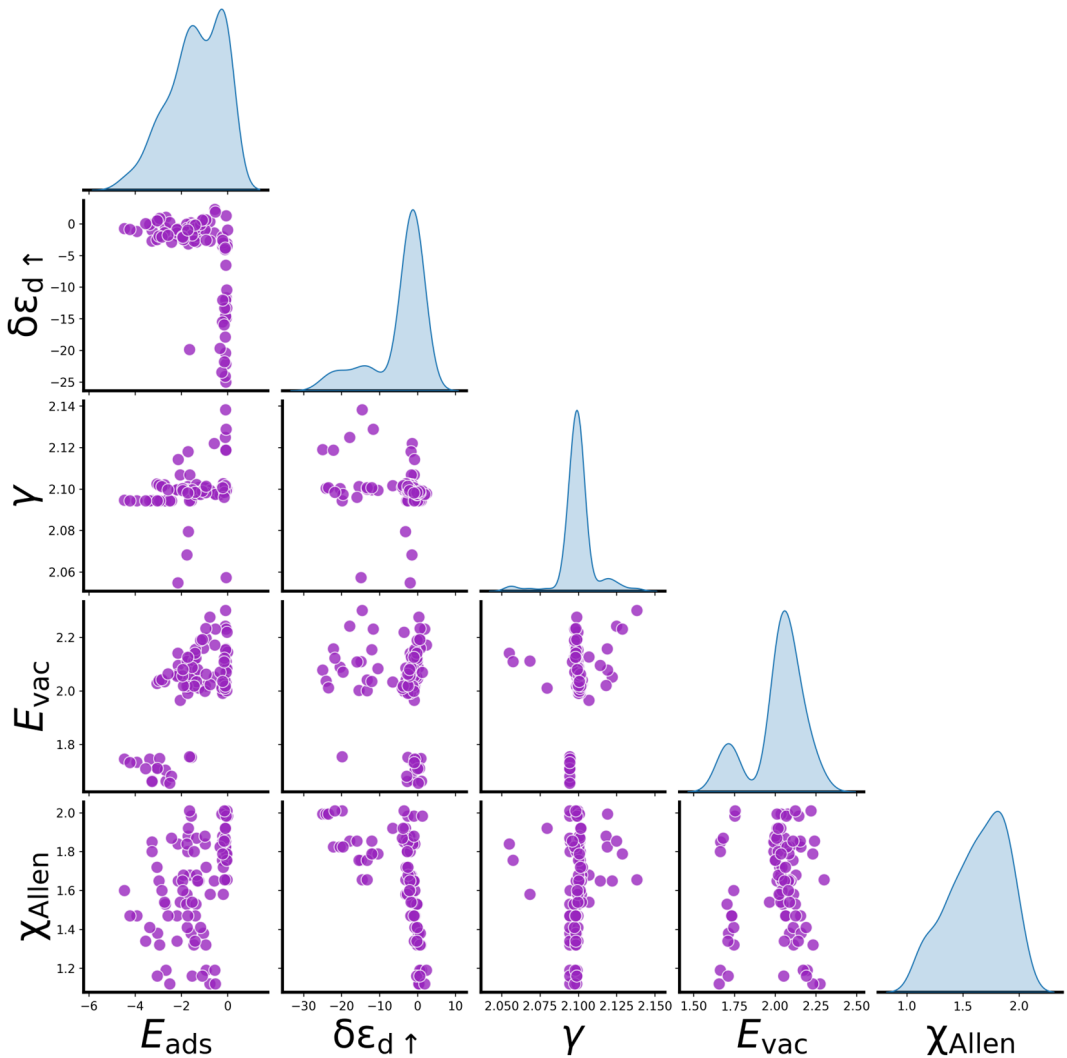


Figure 24: Pairwise Plot of Adsorption Energy and Key Descriptors. This chart displays the pairwise relationships between CO adsorption energy and its four most correlated descriptors: d-band center (spin-up) $\delta\epsilon_d \uparrow$, lattice parameter γ , vacuum level E_{vac} , and electronegativity on the Allen scale χ_{Allen} , identified by Kendall rank correlation analysis. Data from all six substrates investigated in this study are included.

Table 15: Notations for elementary descriptors and electronic descriptors.

	Elementary Descriptors		Electronic Descriptors
R	atomic radius	α, β, γ	lattice parameters
E_{ea}	electron affinity	Φ_{DFT}	DFT calculated work function
Φ	work function	E_{vac}	vacuum level
$\chi_{\text{Allen}}, \chi_{\text{P}}, \chi_{\text{RevP}}$	electronegativity in Allen, Pauling and revised Pauling scales	$E_g, E_g \uparrow, E_g \downarrow$	average, spin-up and spin-down band gaps
A_r	relative atomic mass	e_d	number of d-electrons
E_i	ionization energy	$\delta e_d \uparrow$	d-band centre (spin-up)
G	group number	W_d	d-band width
P	period number	e_{Bader}	Bader charge
V	number of valence electrons		

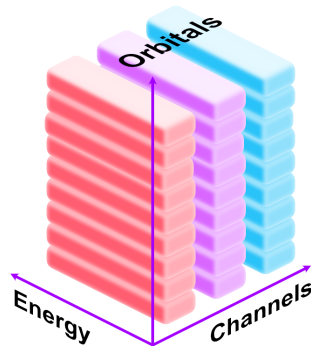


Figure 25: Schematic representation of the input eDOS data structure.

For practical purposes, certain spatial hierarchies are expected to remain invariant, such as the energy range over which the eDOS is sampled. In this work, we maintain a consistent energy range of -14 eV to 6 eV, sampled at a density of 50 points \cdot eV $^{-1}$. In addition to maintaining a fixed energy range, the following steps are taken to standardize the input eDOS data: 1. For atoms lacking d-electrons, the eDOS is zero-padded. 2. f-orbital eDOS data are excluded. 3. The eDOS of adsorbates is zero-padded along the Channels axis to align with the adsorbate that contains the maximum number of atoms, which, in this study, is the $^*\text{OCH}_3$ species. This padded eDOS is then appended to the metal eDOS.

As a result of these preprocessing steps, the input eDOS arrays consistently have a shape of [4000, 9, 6]. This corresponds to 4000 sampling points across the energy range, 9 eDOS orbitals, and 6 atomic channels.

II.4 Hyperparameter tuning for CNN

Table 16: The hyperparameter search space.

Hyperparameter	Search Space	Description
learningRate	$[10^{-4}, 10^{-2}]$, log scale	Learning rate of Adam [31] optimizer
dropoutRate	[0, 1]	Dropout rate
root_fc0	128, 256, 512	Output dimensionality of 1 st fully connected layer in root
root_fc1	256, 512, 1024, 2048	Output dimensionality of 2 nd fully connected layer in root
root_act	“tanh”, “relu”, “sigmoid”	Activation function of fully connected layers in root
kernelSize	[2, 32]	Width of the convolution window
numFilters	[8, 64]	Number of filters in the convolution
numConvLayers	[1, 16]	Number of convolution layers
numConvBlocks	[1, 16]	Number of convolution blocks
br_fc0	16, 32, 64, 128, 256, 512	Output dimensionality of 1 st fully connected layer in branch
br_fc1	8, 16, 32, 64, 128, 256	Output dimensionality of 2 nd fully connected layer in branch
br_act	“tanh”, “relu”, “sigmoid”	Activation function of fully connected layers in branch

II.5 Occlusion experiment

II.6 Shifting experiment

Table 17: Optimal hyperparameters identified with Hyperband algorithm.

Hyperparameter	Optimal Value	Description
learningRate	10^{-3}	Learning rate of Adam [31] optimizer
dropoutRate	0.3	Dropout rate
root_fc0	256	Output dimensionality of 1 st fully connected layer in root
root_fc1	512	Output dimensionality of 2 nd fully connected layer in root
root_act	“relu”	Activation function of fully connected layers in root
kernelSize	10	Width of convolution window
numFilters	17	Number of filters in the convolution
numConvLayers	3	Number of convolution layers
numConvBlocks	1	Number of convolution blocks
br_fc0	256	Output dimensionality of 1 st fully connected layer in branch
br_fc1	128	Output dimensionality of 2 nd fully connected layer in branch
br_act	“tanh”	Activation function of fully connected layers in branch

Table 18: Prediction mean absolute errors of the CNN model.

Adsorbate	Original dataset (eV)	Augmented dataset (eV)
CO ₂	0.0447	0.0336
COOH	0.0436	0.0581
CO	0.0402	0.0402
CHO	0.0614	0.0778
CH ₂ O	0.0553	0.0632
OCH ₃	0.0605	0.0636
O	0.1135	0.1081
OH	0.0547	0.0602
H	0.0703	0.0646

Note: The same CNN model, trained on the augmented dataset, was used for all predictions. The term “original dataset” refers to evaluations conducted on the original dataset without any augmented data; it does not imply the use of a different CNN model trained solely on the original dataset. Similarly, “augmented dataset” refers to evaluations on the dataset with both original data and augment data, not a distinct model.

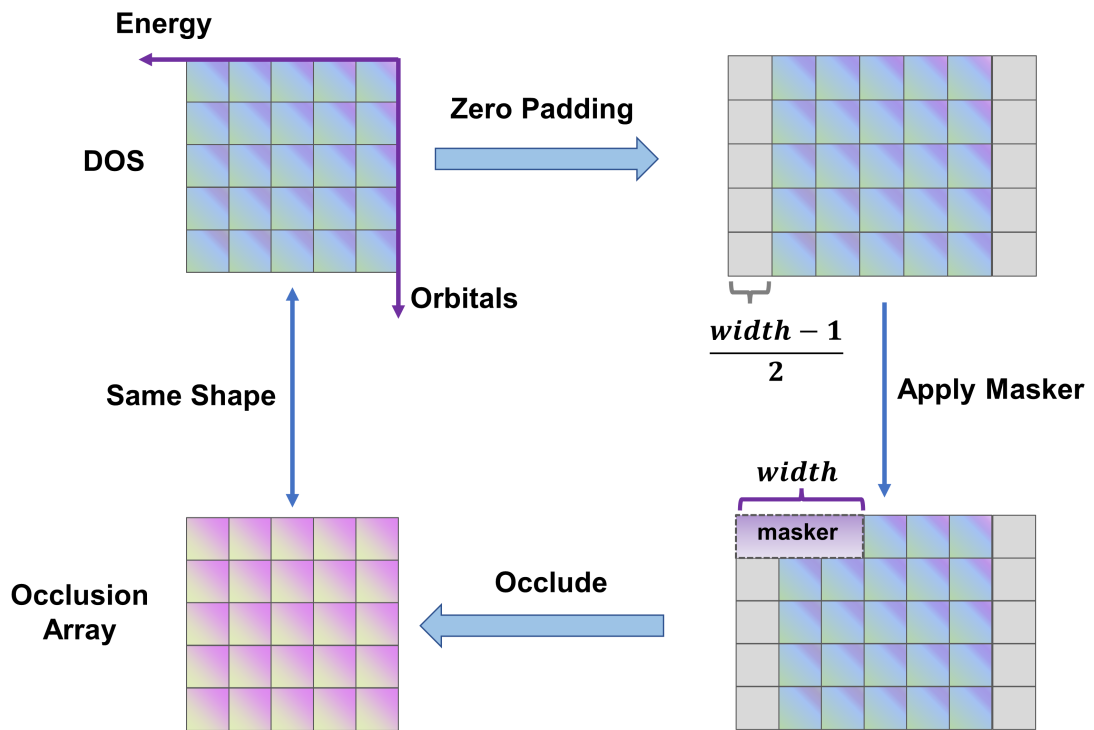


Figure 26: Illustration of the eDOS occlusion experiment. This figure demonstrates the step-by-step process of the occlusion experiment. The input eDOS array first undergoes zero-padded, and then a masker of width “width” is applied, resulting in an occlusion array that preserves the shape of the input array.

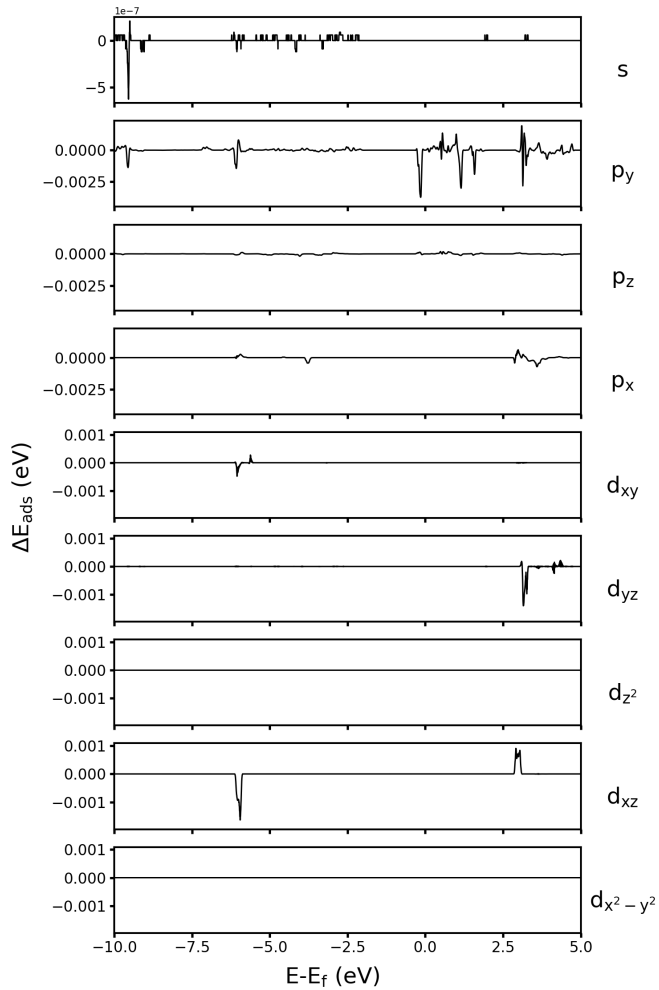


Figure 27: Occlusion Experiment with a masker width of “1”. This figure shows an occlusion experiment on the Ge atom in the initial state of CO adsorption on Ge@g-C₃N₄.

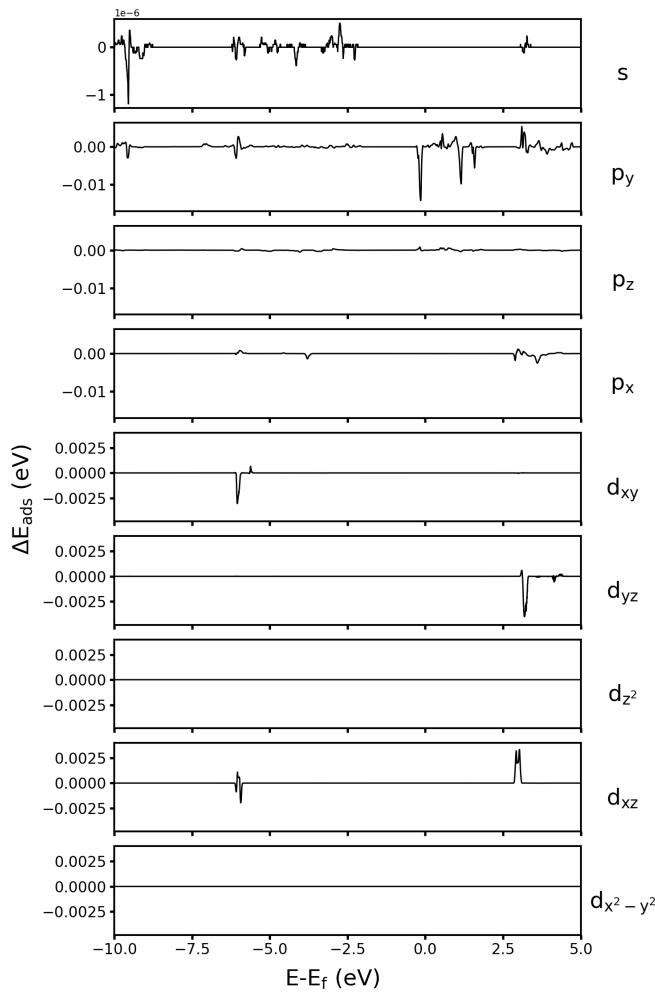


Figure 28: Occlusion Experiment with a masker width of “3”. This figure shows an occlusion experiment on the Ge atom in the initial state of CO adsorption on Ge@g-C₃N₄.

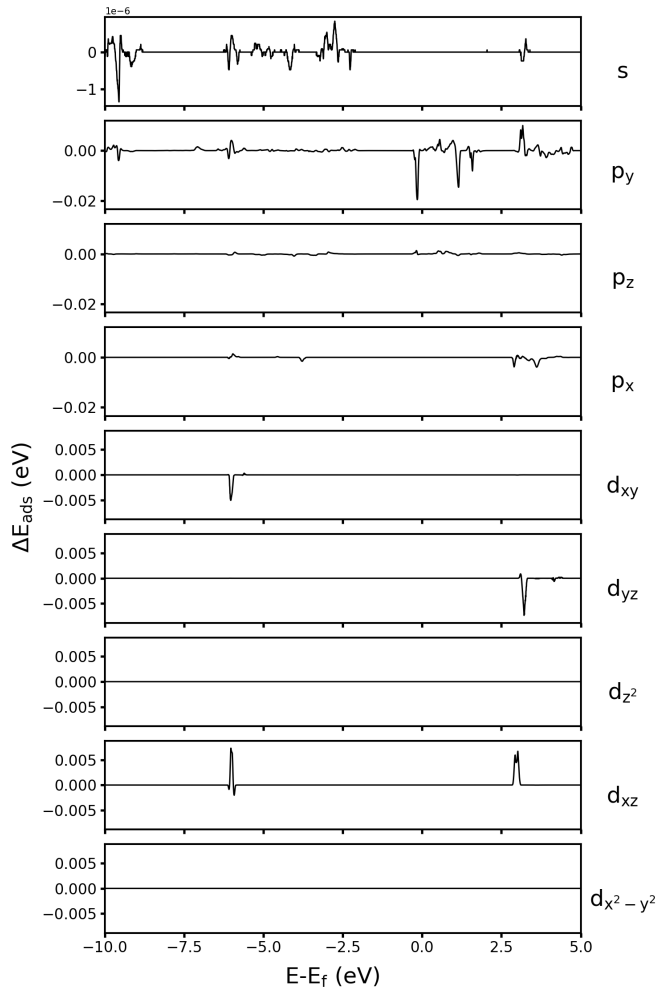


Figure 29: Occlusion Experiment with a masker width of “5”. This figure shows an occlusion experiment on the Ge atom in the initial state of CO adsorption on Ge@g-C₃N₄.

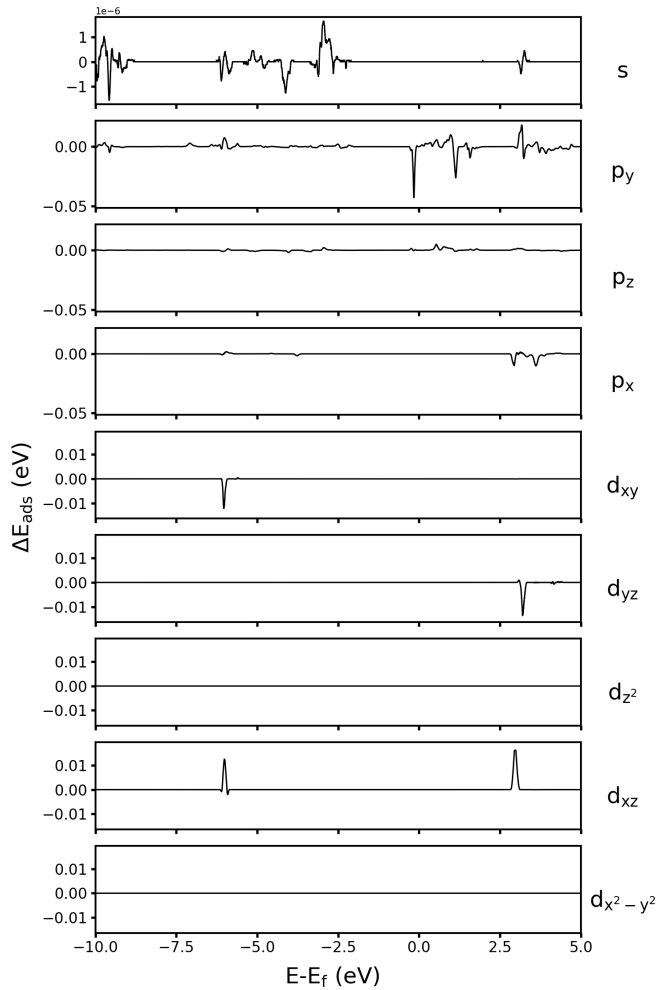


Figure 30: Occlusion Experiment with a masker width of “11”. This figure shows an occlusion experiment on the Ge atom in the initial state of CO adsorption on Ge@g-C₃N₄.

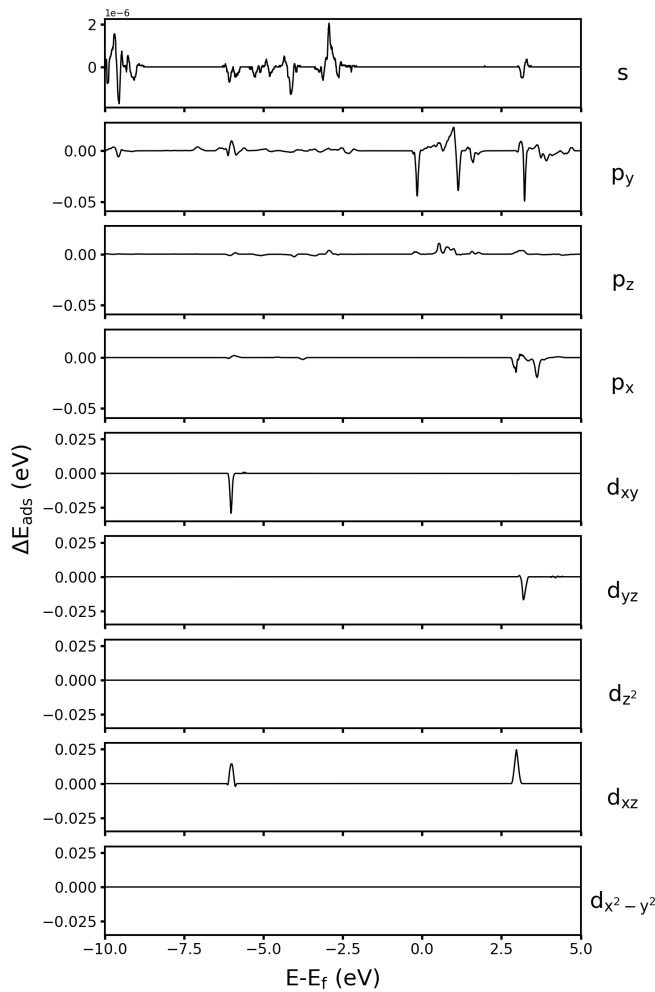


Figure 31: Occlusion Experiment with a masker width of “21”. This figure shows an occlusion experiment on the Ge atom in the initial state of CO adsorption on Ge@g-C₃N₄.

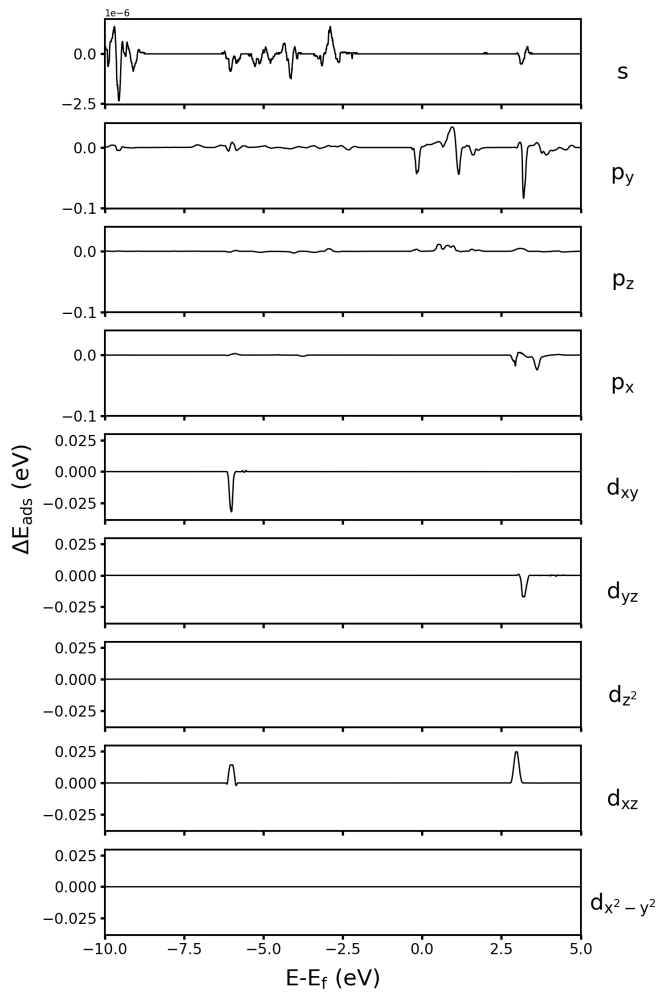


Figure 32: Occlusion Experiment with a masker width of “31”. This figure shows an occlusion experiment on the Ge atom in the initial state of CO adsorption on Ge@g-C₃N₄.

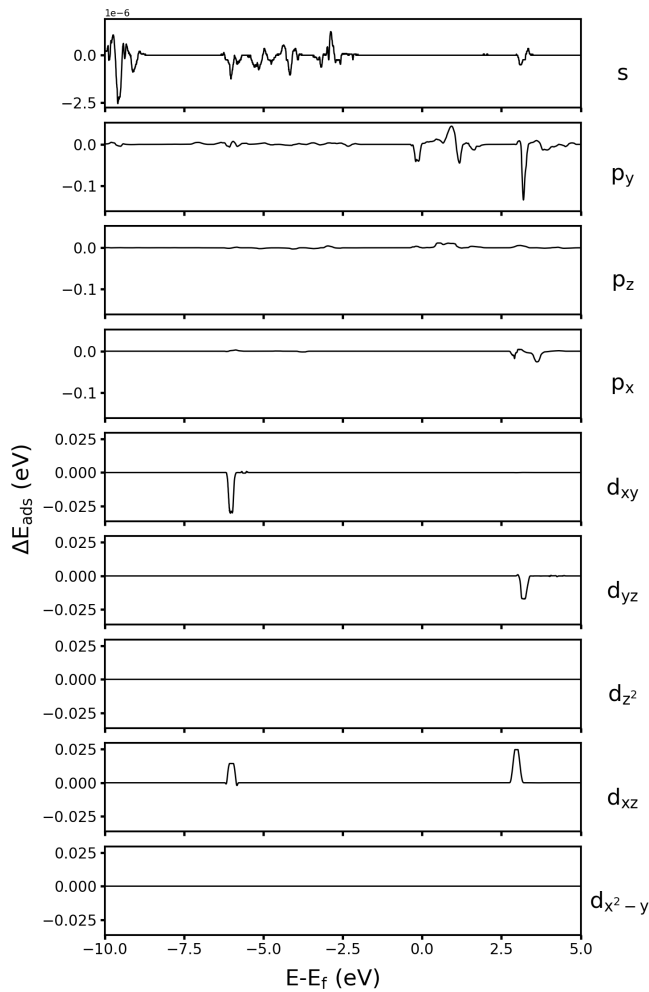


Figure 33: Occlusion Experiment with a masker width of “41”. This figure shows an occlusion experiment on the Ge atom in the initial state of CO adsorption on Ge@g-C₃N₄.

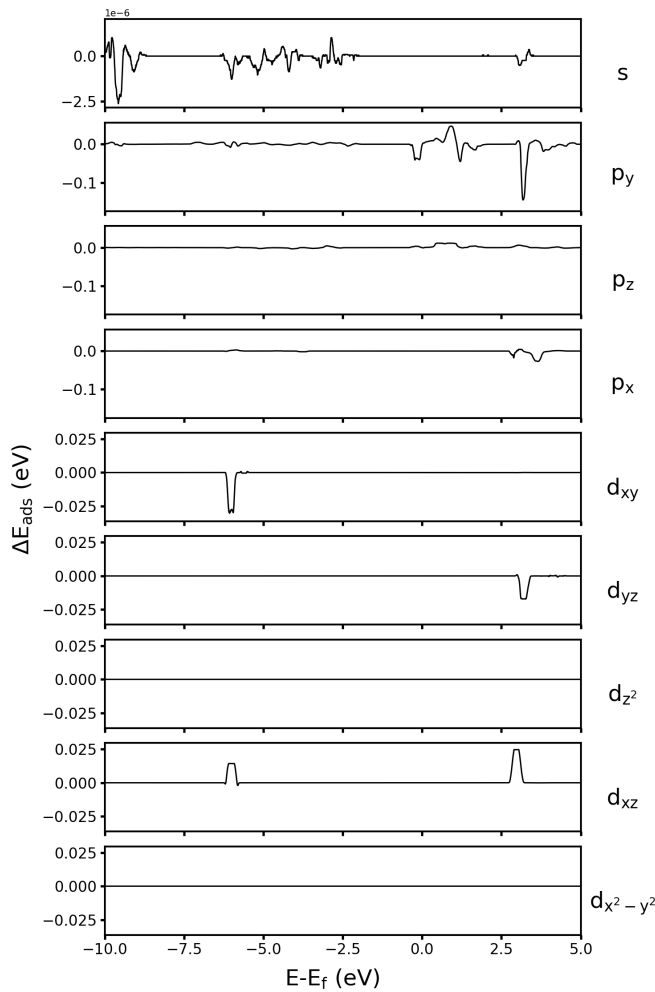


Figure 34: Occlusion Experiment with a masker width of “51”. This figure shows an occlusion experiment on the Ge atom in the initial state of CO adsorption on Ge@g-C₃N₄.

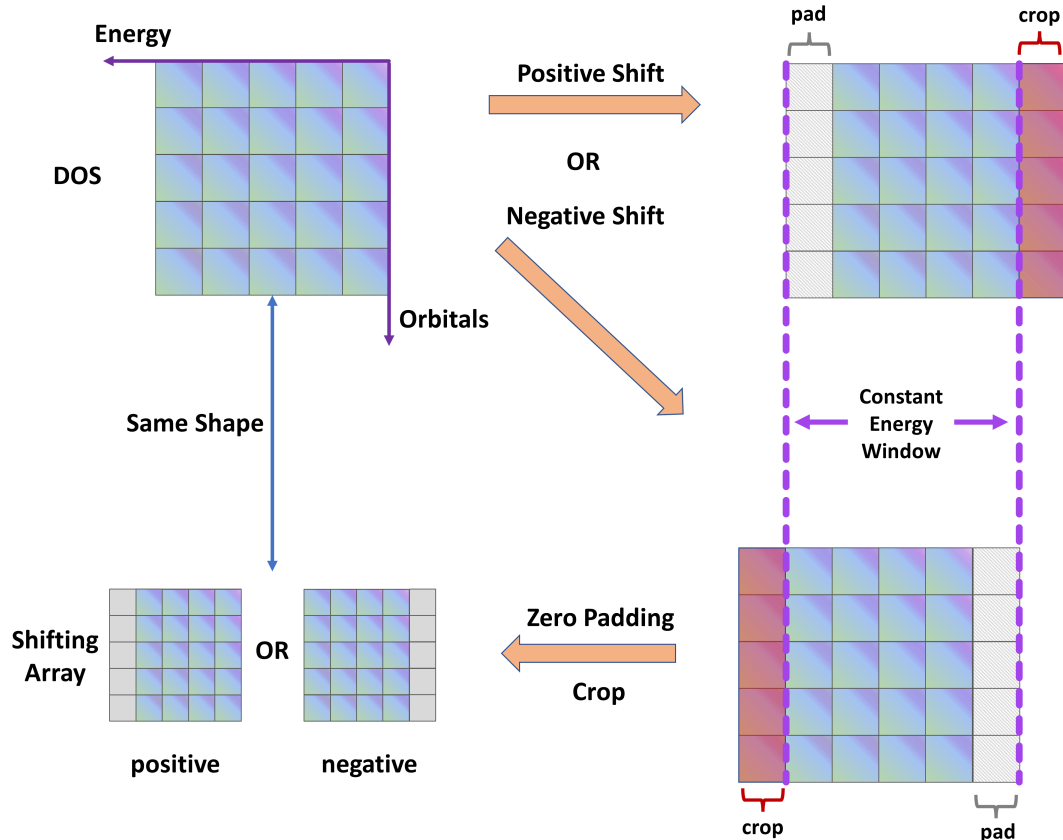


Figure 35: Illustration of the eDOS shifting experiment. This figure illustrates the sequential stages of the shifting experiment. Initially, the input eDOS array is shifted along the Energy axis. Subsequently, it undergoes zero-padding and cropping, ensuring a consistent shape based on the shifting direction, to match the input eDOS array. The resulting shifted array is then processed by the CNN model to assess the disturbance in adsorption energy caused by the shifting operation.

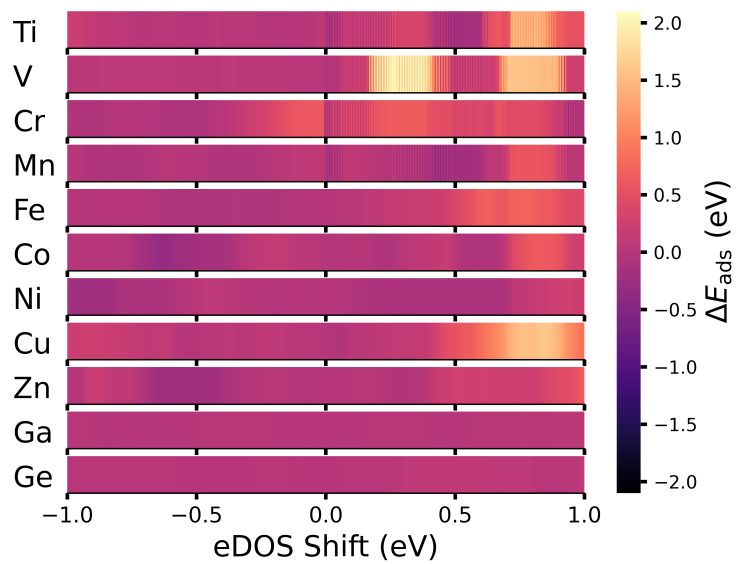


Figure 36: Shifting experiment on p orbital. Effect of orbital shifting on CO adsorption energy, predicted by the CNN model, for single metal atom catalysts supported on g-C₃N₄. The perturbations caused by shifting of entire p orbital are presented. The shifting step size corresponds to the energy resolution of the eDOS, set at 0.005 eV in this study. A positive eDOS shift indicates a shift towards higher energy levels, and vice versa.

III Other additional information

III.1 Additional information on machine learning environment

The hyperparameter optimization for the proposed CNN model was performed using NVIDIA® V100 Tensor Core GPUs, courtesy of the Australian National Computational Infrastructure’s (NCI) HPC Gadi system. The HyperBand algorithm [41], as implemented in KerasTuner [50], facilitated the tuning process.

Table 19: Core packages in the deep learning environment.

Name	Version	Build	Channel
conda	4.13.0	py39h06a4308_0	anaconda
cuda-nvcc	11.8.89	0	nvidia
cuda-toolkit	11.8.0	0	nvidia
cudatoolkit	11.6.0	habf752d_9	nvidia
ipykernel	6.9.1	py39h06a4308_0	anaconda
ipython	7.34.0	pypi_0	pypi
jupyter_client	7.2.2	py39h06a4308_0	anaconda
jupyterlab	3.4.4	py39h06a4308_0	anaconda
keras	2.9.0	pypi_0	pypi
keras-preprocessing	1.1.2	pypi_0	pypi
keras-tuner	1.3.5		pypi
matplotlib	3.5.1	py39h06a4308_1	anaconda
numpy	1.22.4	pypi_0	pypi
pandas	1.3.4	py39h8c16a72_0	anaconda
python	3.9.12	h12debd9_1	anaconda
scikit-learn	1.1.1	py39h6a678d5_0	anaconda
scipy	1.8.1	py39hddc5342_3	conda-forge
tensorboard	2.9.1	pypi_0	pypi
tensorflow	2.9.3	pypi_0	pypi
tensorflow-gpu	2.9.3	pypi_0	pypi
xlrd	2.0.1	pyhd3eb1b0_0	anaconda
yaml	0.2.5	h7b6447c_0	anaconda

Note: The complete list of packages is provided along with the source code.

III.2 Additional information on data analysis and visualization environment

Data analysis and visualization tasks were executed on an Apple MacBook Air featuring an octa-core M2 chip. For accuracy, the TensorFlow-Metal plugin for Mac-based GPU acceleration was deliberately excluded, as it could potentially yield erroneous CNN model predictions.

The illustrations of CNN architecture displayed in Figure 1 of the main text, as well as Figure 26 and Figure 35, were obtained from the GitHub repository dair-ai/ml-visuals [56]. Blender was used to create and render the visual representation of the catalyst analysis pipeline shown in Figure 1 of the main text.

Table 20: Core packages in data analysis and visualization environment.

Name	Version	Build	Channel
bokeh	3.2.2	pypi_0	pypi
colorcet	3.0.1	pypi_0	pypi
heatmapz	0.0.4	pypi_0	pypi
keras	2.13.1	pypi_0	pypi
keras-tuner	1.3.5	pypi_0	pypi
matplotlib	3.7.2	pypi_0	pypi
numpy	1.24.3	pypi_0	pypi
pandas	2.0.3	pypi_0	pypi
python	3.11.4	hb885b13_0	
pyyaml	6.0.1	pypi_0	pypi
scikit-learn	1.3.0	pypi_0	pypi
scipy	1.11.1	pypi_0	pypi
seaborn	0.12.2	pypi_0	pypi
tensorboard	2.13.0	pypi_0	pypi
tensorflow	2.13.0	pypi_0	pypi
tensorflow-macos	2.13.0	pypi_0	pypi

Note: The complete list of packages is provided along with the source code.

References

- [1] Martín Abadi, Paul Barham, Jianmin Chen, Zhifeng Chen, Andy Davis, Jeffrey Dean, Matthieu Devin, Sanjay Ghemawat, Geoffrey Irving, Michael Isard, et al. {TensorFlow}: a system for {Large-Scale} machine learning. In *12th USENIX symposium on operating systems design and implementation (OSDI 16)*, pages 265–283, 2016.
- [2] Frank Abild-Pedersen, Jeff Greeley, Felix Studt, Jan Rossmeisl, Ture R Munter, Poul Georg Moses, Egill Skulason, Thomas Bligaard, and Jens Kehlet Nørskov. Scaling properties of adsorption energies for hydrogen-containing molecules on transition-metal surfaces. *Physical review letters*, 99(1):016105, 2007.
- [3] AA Balandin. Modern state of the multiplet theor of heterogeneous catalysis. *Advances in catalysis*, 19:1–210, 1969.
- [4] Bapi Bera, Arup Chakraborty, Tathagata Kar, Pradipkumar Leuaa, and Manoj Neergat. Density of states, carrier concentration, and flat band potential derived from electrochemical impedance measurements of n-doped carbon and their influence on electrocatalysis of oxygen reduction reaction. *The Journal of Physical Chemistry C*, 121(38):20850–20856, 2017.
- [5] Peter E Blöchl, Ove Jepsen, and Ole Krogh Andersen. Improved tetrahedron method for brillouin-zone integrations. *Physical Review B*, 49(23):16223, 1994.
- [6] Yanming Cai, Jiaju Fu, Yang Zhou, Yu-Chung Chang, Qianhao Min, Jun-Jie Zhu, Yuehe Lin, and Wenlei Zhu. Insights on forming n, o-coordinated cu single-atom catalysts for electrochemical reduction co₂ to methane. *Nature Communications*, 12(1):586, 2021.
- [7] Emily A Carter. Challenges in modeling materials properties without experimental input. *Science*, 321(5890):800–803, 2008.
- [8] Anand Chandrasekaran, Deepak Kamal, Rohit Batra, Chiho Kim, Lihua Chen, and Rampi Ramprasad. Solving the electronic structure problem with machine learning. *npj Computational Materials*, 5(1):22, 2019.
- [9] Yalu Chen, Yufeng Huang, Tao Cheng, and William A Goddard III. Identifying active sites for co₂ reduction on dealloyed gold surfaces by combining machine learning with multiscale simulations. *Journal of the American Chemical Society*, 141(29):11651–11657, 2019.

- [10] Beatriz Roldan Cuenya and Farzad Behafarid. Nanocatalysis: size-and shape-dependent chemisorption and catalytic reactivity. *Surface Science Reports*, 70(2):135–187, 2015.
- [11] Volker L Deringer, Andrei L Tchougréeff, and Richard Dronskowski. Crystal orbital hamilton population (cohp) analysis as projected from plane-wave basis sets. *The journal of physical chemistry A*, 115(21):5461–5466, 2011.
- [12] Olaf Deutschmann, Helmut Knözinger, Karl Kochloefl, and Thomas Turek. Heterogeneous catalysis and solid catalysts, 1. fundamentals. *Ullmann's encyclopedia of industrial chemistry*, 2000.
- [13] Giovanni Di Liberto, Luis A Cipriano, and Gianfranco Pacchioni. Universal principles for the rational design of single atom electrocatalysts? handle with care. *ACS Catalysis*, 12(10):5846–5856, 2022.
- [14] Cao-Thang Dinh, Thomas Burdyny, Md Golam Kibria, Ali Seifitokaldani, Christine M Gabardo, F Pelayo García de Arquer, Amirreza Kiani, Jonathan P Edwards, Phil De Luna, Oleksandr S Bushuyev, et al. Co₂ electroreduction to ethylene via hydroxide-mediated copper catalysis at an abrupt interface. *Science*, 360(6390):783–787, 2018.
- [15] Richard Dronskowski and Peter E Blöchl. Crystal orbital hamilton populations (cohp): energy-resolved visualization of chemical bonding in solids based on density-functional calculations. *The Journal of Physical Chemistry*, 97(33):8617–8624, 1993.
- [16] William J Durand, Andrew A Peterson, Felix Studt, Frank Abild-Pedersen, and Jens K Nørskov. Structure effects on the energetics of the electrochemical reduction of co₂ by copper surfaces. *Surface Science*, 605(15-16):1354–1359, 2011.
- [17] Jeremy T Feaster, Chuan Shi, Etosha R Cave, Toru Hatsukade, David N Abram, Kendra P Kuhl, Christopher Hahn, Jens K Nørskov, and Thomas F Jaramillo. Understanding selectivity for the electrochemical reduction of carbon dioxide to formic acid and carbon monoxide on metal electrodes. *Acs Catalysis*, 7(7):4822–4827, 2017.
- [18] Victor Fung, Guoxiang Hu, Panchapakesan Ganesh, and Bobby G Sumpter. Machine learned features from density of states for accurate adsorption energy prediction. *Nature communications*, 12(1):88, 2021.

- [19] Victor Fung, Guoxiang Hu, Zili Wu, and De-en Jiang. Descriptors for hydrogen evolution on single atom catalysts in nitrogen-doped graphene. *The Journal of Physical Chemistry C*, 124(36):19571–19578, 2020.
- [20] Bryan R. Goldsmith, Jacques Esterhuizen, Jin-Xun Liu, Christopher J. Bartel, and Christopher Sutton. Machine learning for heterogeneous catalyst design and discovery. *AIChe Journal*, 64(7):2311–2323, 2018.
- [21] Akansha Goyal, Giulia Marcandalli, Vladislav A Mints, and Marc TM Koper. Competition between co₂ reduction and hydrogen evolution on a gold electrode under well-defined mass transport conditions. *Journal of the American Chemical Society*, 142(9):4154–4161, 2020.
- [22] BJKN Hammer and Jens K Nørskov. Electronic factors determining the reactivity of metal surfaces. *Surface science*, 343(3):211–220, 1995.
- [23] Bjørk Hammer and Jens Kehlet Nørskov. Theoretical surface science and catalysis-calculations and concepts. In *Advances in catalysis*, volume 45, pages 71–129. Elsevier, 2000.
- [24] Zhong-Kang Han, Debalaya Sarker, Runhai Ouyang, Aliaksei Mazheika, Yi Gao, and Sergey V Levchenko. Single-atom alloy catalysts designed by first-principles calculations and artificial intelligence. *Nature communications*, 12(1):1833, 2021.
- [25] Hai-Cai Huang, Yang Zhao, Jing Wang, Jun Li, Jing Chen, Qiang Fu, Yu-Xiang Bu, and Shi-Bo Cheng. Rational design of an efficient descriptor for single-atom catalysts in the hydrogen evolution reaction. *Journal of Materials Chemistry A*, 8(18):9202–9208, 2020.
- [26] Yan Jiao, Yao Zheng, Ping Chen, Mietek Jaroniec, and Shi-Zhang Qiao. Molecular scaffolding strategy with synergistic active centers to facilitate electrocatalytic co₂ reduction to hydrocarbon/alcohol. *Journal of the American Chemical Society*, 139(49):18093–18100, 2017.
- [27] Ryosuke Jinnouchi and Ryoji Asahi. Predicting catalytic activity of nanoparticles by a dft-aided machine-learning algorithm. *The journal of physical chemistry letters*, 8(17):4279–4283, 2017.
- [28] Wen Ju, Alexander Bagger, Guang-Ping Hao, Ana Sofia Varela, Ilya Sinev, Volodymyr Bon, Beatriz Roldan Cuenya, Stefan Kaskel, Jan Rossmeisl, and Peter Strasser. Understanding activity and selectivity of metal-nitrogen-doped carbon catalysts for electrochemical reduction of co₂. *Nature communications*, 8(1):944, 2017.

- [29] Seiji Kajita, Nobuko Ohba, Ryosuke Jinnouchi, and Ryoji Asahi. A universal 3d voxel descriptor for solid-state material informatics with deep convolutional neural networks. *Scientific reports*, 7(1):16991, 2017.
- [30] Maurice G Kendall. A new measure of rank correlation. *Biometrika*, 30(1/2):81–93, 1938.
- [31] Diederik P. Kingma and Jimmy Ba. Adam: A method for stochastic optimization, 2017.
- [32] Scott Kirklin, James E Saal, Bryce Meredig, Alex Thompson, Jeff W Doak, Muratahan Aykol, Stephan Rühl, and Chris Wolverton. The open quantum materials database (oqmd): assessing the accuracy of dft formation energies. *npj Computational Materials*, 1(1):1–15, 2015.
- [33] Toshikatsu Koga, Katsutoshi Kanayama, Shinya Watanabe, and Ajit J Thakkar. Analytical hartree–fock wave functions subject to cusp and asymptotic constraints: He to xe, li+ to cs+, h- to i-. *International journal of quantum chemistry*, 71(6):491–497, 1999.
- [34] Adam Kortylewski, Qing Liu, Huiyu Wang, Zhishuai Zhang, and Alan Yuille. Combining compositional models and deep networks for robust object classification under occlusion. In *Proceedings of the IEEE/CVF winter conference on applications of computer vision*, pages 1333–1341, 2020.
- [35] Georg Kresse and Jürgen Furthmüller. Efficiency of ab-initio total energy calculations for metals and semiconductors using a plane-wave basis set. *Computational materials science*, 6(1):15–50, 1996.
- [36] Georg Kresse and Jürgen Furthmüller. Efficient iterative schemes for ab initio total-energy calculations using a plane-wave basis set. *Physical review B*, 54(16):11169, 1996.
- [37] Georg Kresse and Jürgen Hafner. Ab initio molecular dynamics for liquid metals. *Physical review B*, 47(1):558, 1993.
- [38] Alex Krizhevsky, Ilya Sutskever, and Geoffrey E Hinton. Imagenet classification with deep convolutional neural networks. In F. Pereira, C.J. Burges, L. Bottou, and K.Q. Weinberger, editors, *Advances in Neural Information Processing Systems*, volume 25. Curran Associates, Inc., 2012.
- [39] Kohei Kusada, Dongshuang Wu, Tomokazu Yamamoto, Takaaki Toriyama, Syo Matsumura, Wei Xie, Michihisa Koyama, Shogo Kawaguchi, Yoshiki Kubota, and Hiroshi Kitagawa. Emergence of high orr activity through control-

- ling local density-of-states by alloying immiscible au and ir. *Chemical science*, 10(3):652–656, 2019.
- [40] Kurt Lejaeghere, Gustav Bihlmayer, Torbjörn Björkman, Peter Blaha, Stefan Blügel, Volker Blum, Damien Caliste, Ivano E Castelli, Stewart J Clark, Andrea Dal Corso, et al. Reproducibility in density functional theory calculations of solids. *Science*, 351(6280):aad3000, 2016.
 - [41] Lisha Li, Kevin Jamieson, Giulia DeSalvo, Afshin Rostamizadeh, and Ameet Talwalkar. Hyperband: A novel bandit-based approach to hyperparameter optimization. *Journal of Machine Learning Research*, 18(185):1–52, 2018.
 - [42] Guiji Liu, Michelle Lee, Soonho Kwon, Guosong Zeng, Johanna Eichhorn, Aya K Buckley, F Dean Toste, William A Goddard III, and Francesca M Toma. Co₂ reduction on pure cu produces only h₂ after subsurface o is depleted: theory and experiment. *Proceedings of the National Academy of Sciences*, 118(23):e2012649118, 2021.
 - [43] Stefan Maintz, Volker L Deringer, Andrei L Tchougréeff, and Richard Dronskowski. Analytic projection from plane-wave and paw wavefunctions and application to chemical-bonding analysis in solids. *Journal of computational chemistry*, 34(29):2557–2567, 2013.
 - [44] Stefan Maintz, Volker L Deringer, Andrei L Tchougréeff, and Richard Dronskowski. Lobster: A tool to extract chemical bonding from plane-wave based dft, 2016.
 - [45] Koichi Momma and Fujio Izumi. Vesta: a three-dimensional visualization system for electronic and structural analysis. *Journal of Applied crystallography*, 41(3):653–658, 2008.
 - [46] Ryky Nelson, Christina Ertural, Janine George, Volker L Deringer, Geoffroy Hautier, and Richard Dronskowski. Lobster: Local orbital projections, atomic charges, and chemical-bonding analysis from projector-augmented-wave-based density-functional theory. *Journal of Computational Chemistry*, 41(21):1931–1940, 2020.
 - [47] Xiaowa Nie, Wenjia Luo, Michael J Janik, and Aravind Asthagiri. Reaction mechanisms of co₂ electrochemical reduction on cu (1 1 1) determined with density functional theory. *Journal of catalysis*, 312:108–122, 2014.
 - [48] Jens K Nørskov, Frank Abild-Pedersen, Felix Studt, and Thomas Bligaard. Density functional theory in surface chemistry and catalysis. *Proceedings of the National Academy of Sciences*, 108(3):937–943, 2011.

- [49] Jens Kehlet Nørskov, Jan Rossmeisl, Ashildur Logadottir, LRKJ Lindqvist, John R Kitchin, Thomas Bligaard, and Hannes Jonsson. Origin of the overpotential for oxygen reduction at a fuel-cell cathode. *The Journal of Physical Chemistry B*, 108(46):17886–17892, 2004.
- [50] Tom O’Malley, Elie Bursztein, James Long, François Chollet, Haifeng Jin, Luca Invernizzi, et al. Kerastuner. <https://github.com/keras-team/keras-tuner>, 2019.
- [51] Silvio Osella and William A Goddard III. Co₂ reduction to methane and ethylene on a single-atom catalyst: A grand canonical quantum mechanics study. *Journal of the American Chemical Society*, 145(39):21319–21329, 2023.
- [52] John P Perdew, Kieron Burke, and Matthias Ernzerhof. Generalized gradient approximation made simple. *Physical review letters*, 77(18):3865, 1996.
- [53] Andrew A Peterson, Frank Abild-Pedersen, Felix Studt, Jan Rossmeisl, and Jens K Nørskov. How copper catalyzes the electroreduction of carbon dioxide into hydrocarbon fuels. *Energy & Environmental Science*, 3(9):1311–1315, 2010.
- [54] Andrew A Peterson and Jens K Nørskov. Activity descriptors for co₂ electroreduction to methane on transition-metal catalysts. *The Journal of Physical Chemistry Letters*, 3(2):251–258, 2012.
- [55] Wenhao Ren, Xin Tan, Wanfeng Yang, Chen Jia, Shumao Xu, Kaixue Wang, Sean C Smith, and Chuan Zhao. Isolated diatomic ni-fe metal–nitrogen sites for synergistic electroreduction of co₂. *Angewandte Chemie International Edition*, 58(21):6972–6976, 2019.
- [56] Elvis Saravia. ML Visuals. <https://github.com/dair-ai/ml-visuals>, December 2021.
- [57] Neil Savage. Breaking into the black box of artificial intelligence, 2022.
- [58] Richard Socher, Brody Huval, Bharath Bath, Christopher D Manning, and Andrew Ng. Convolutional-recursive deep learning for 3d object classification. *Advances in neural information processing systems*, 25, 2012.
- [59] Zhongti Sun, Zhilong Song, and Wan-Jian Yin. Going beyond the d-band center to describe co₂ activation on single-atom alloys. *Advanced Energy and Sustainability Research*, 3(2):2100152, 2022.

- [60] Ichigaku Takigawa, Ken-ichi Shimizu, Koji Tsuda, and Satoru Takakusagi. Machine-learning prediction of the d-band center for metals and bimetals. *RSC advances*, 6(58):52587–52595, 2016.
- [61] Hari Thirumalai and John R Kitchin. Investigating the reactivity of single atom alloys using density functional theory. *Topics in Catalysis*, 61:462–474, 2018.
- [62] Du Tran, Lubomir Bourdev, Rob Fergus, Lorenzo Torresani, and Manohar Paluri. Learning spatiotemporal features with 3d convolutional networks, 2015.
- [63] Aiqin Wang, Jun Li, and Tao Zhang. Heterogeneous single-atom catalysis. *Nature Reviews Chemistry*, 2(6):65–81, 2018.
- [64] Angtian Wang, Yihong Sun, Adam Kortylewski, and Alan L Yuille. Robust object detection under occlusion with context-aware compositionalnets. In *Proceedings of the IEEE/CVF Conference on Computer Vision and Pattern Recognition*, pages 12645–12654, 2020.
- [65] Vei Wang, Nan Xu, Jin-Cheng Liu, Gang Tang, and Wen-Tong Geng. Vaspkit: A user-friendly interface facilitating high-throughput computing and analysis using vasp code. *Computer Physics Communications*, 267:108033, 2021.
- [66] Kuba Weimann and Tim OF Conrad. Transfer learning for ecg classification. *Scientific reports*, 11(1):5251, 2021.
- [67] Jess Wellendorff, Trent L. Silbaugh, Delfina Garcia-Pintos, Jens K. Nørskov, Thomas Bligaard, Felix Studt, and Charles T. Campbell. A benchmark database for adsorption bond energies to transition metal surfaces and comparison to selected dft functionals. *Surface Science*, 640:36–44, 2015. Reactivity Concepts at Surfaces: Coupling Theory with Experiment.
- [68] Yutong Xie, Ziqiao Xu, Jiaqi Ma, and Qiaozhu Mei. How much of the chemical space has been covered? measuring and improving the variety of candidate set in molecular generation. *CoRR*, abs/2112.12542, 2021.
- [69] Hong Bin Yang, Sung-Fu Hung, Song Liu, Kaidi Yuan, Shu Miao, Liping Zhang, Xiang Huang, Hsin-Yi Wang, Weizheng Cai, Rong Chen, et al. Atomically dispersed ni (i) as the active site for electrochemical co₂ reduction. *Nature energy*, 3(2):140–147, 2018.
- [70] Hao Yuan, Zhenyu Li, Xiao Cheng Zeng, and Jinlong Yang. Descriptor-based design principle for two-dimensional single-atom catalysts: carbon dioxide

- electroreduction. *The journal of physical chemistry letters*, 11(9):3481–3487, 2020.
- [71] Matthew D Zeiler and Rob Fergus. Visualizing and understanding convolutional networks. In *Computer Vision–ECCV 2014: 13th European Conference, Zurich, Switzerland, September 6–12, 2014, Proceedings, Part I 13*, pages 818–833. Springer, 2014.
 - [72] Quan-shi Zhang and Song-Chun Zhu. Visual interpretability for deep learning: a survey. *Frontiers of Information Technology & Electronic Engineering*, 19(1):27–39, 2018.
 - [73] Quanshi Zhang, Ying Nian Wu, and Song-Chun Zhu. Interpretable convolutional neural networks. In *Proceedings of the IEEE conference on computer vision and pattern recognition*, pages 8827–8836, 2018.
 - [74] Qing Zhao, John Mark P Martirez, and Emily A Carter. Revisiting understanding of electrochemical co₂ reduction on cu (111): competing proton-coupled electron transfer reaction mechanisms revealed by embedded correlated wavefunction theory. *Journal of the American Chemical Society*, 143(16):6152–6164, 2021.